Segmented Leg Design in Robotics

Master Thesis

Lorenz Küchler

January 29, 2010

Assistant:
Alexander Spröwitz

Biologically Inspired Robotics Group (BIRG)
Prof. Auke Jan Ijspeert

EPFL

Faculté Sciences et Techniques de l'Ingénieur (STI)
Institut de microtechnique (IMT)

Contents

Segmented Leg Design In Robots

Master project, task description

Lorenz Kuchler, September 28, 2009

This master project (17 weeks) aims at a continuation of the work of several BIRG students around the Cheetah robot ([1], [2] and [3]), with the initial emphasis on building a monopod-hopping robot with a segmented leg in simulation and later in hardware. BIRG has built a quadruped robot with passive compliant legs [4]. Cheetah was controlled by a Central Pattern Generator (CPG), developed by Ludovic RIGHETTI ([5], [4]).

The goal of this project is to test three-, two-segmented and telescopic robotic leg designs for their "intrinsic" stability, e.g. their ability to return to cyclic locomotion patters after a disturbance input without altering the control input. Leg design parameters can be the amount of compliant elements, segmentation characteristics, direction (keyword "directional compliance") and characteristics of the compliant elements (e.g. linear springs, nonlinear springs, torsional springs etc.).

Task- and rough timetable-list:

1) Literature review and Webots model recovery
   - Choose between the previous Webots model made by [2] and [3], and Alexandre (current Master project)
   - Literature review on *passive dynamic walkers* (with and without "knee", with compliance)
   - Literature review on the student projects at BIRG concerning the above topic
   - Literature review for segmented legs in Biology and Robotics
   - Decide for a Webots model, come up with a design for the necessary experiments, keywords: internal and external sensor implementation, simple control framework, data acquisition
2) Detailed experiments with the above setup in Webots, data acquisition, detailed analysis
3) Transfer the Webots experimental setup to a real-robot monopod hopper setup, help with electronics, CAD and programming
4) Evaluation of the final leg design in a bounding quadruped robot in Webots, data acquisition, data analysis. Aim is the energetic analysis and the analysis of robustness (e.g. pitching behavior of the robot)

Deliverables:

1) A schedule including the above points as milestones, the mid-defense, the final submission date and the final presentation date.
2) Code, models and software with documentation on CD.
3) Videos on CD.
4) A final report.
5) An entry on the BIRG site, which summarizes the work on the project.

REFERENCES

[1] S. Rutishauser, "Cheetah: compliant quadruped robot," Biologically Inspired Robotic Group, Tech. Rep., 2008.
[2] M. Riess, "Development and test of a model for the cheetah robot," Biologically inspired Robotic Group, Tech. Rep., 2008.
[3] I. Kviatkevitch, "Locomotion exploiting body dynamics on the cheetah robot," Biologically Inspired Robotic Group, Tech. Rep., 2009.
[4] S. Rutishauser, A. Sproewitz, L. Righetti, and A. Ijspeert, "Passive compliant quadruped robot using central pattern generators for locomotion control," in *2008 IEEE International Conference on BiomedicalRobotics and Biomechatronics*, October 2008, conference.
[5] L. Righetti and A. J. Ijspeert, "Pattern generators with sensory feedback for the control of quadruped locomotion," in *Proc. IEEE International Conference on Robotics and Automation ICRA 2008*, 19–23 May 2008, pp. 819–824.

Abstract

This master project aims at a continuation of the work around the Cheetah robot, a quadruped robot with passive compliant legs. The Cheetah's legs are three-segmented pantograph legs featuring a linear spring. The running stability for different pantograph leg designs is investigated in a fully passive, energy conservative physical model. The effect of preloading the spring is examined as well. Furthermore a model for the pantograph leg whithout the restriction of energy conservation is presented. The model aims to achieve stable running by controlling the pantograph leg. The leg angle can be controlled by a motor at the hip in series with a compliance. Stable running is possible, if the system energy is held constant. For this purpose a strategy able to control the system energy by changing the leg length at lift-off is presented.

Chapter 1

Introduction

The goal of this master project is to improve the leg design of the Cheetah robot ([16], [22], [24] and [25]). For this purpose segmented and telescopic robotic leg designs are tested for their "intrinsic" stability. Cheetah features three-segmented legs with passive compliant knee joints. Each leg has two degrees of freedom: knee and hip joint can be actuated. The leg of the Cheetah robot is a pantograph leg i.e. the first (foot/lower arm) and the third leg segment (thigh/scapula) are forced parallel. This is justified by the fact that these segments are indeed nearly parallel for small mammals during walking and running ([10]). The use of compliance in legged systems has the advantage, that the leg can temporarily store and release mechanical energy during the stance phase ([7]).
Fundamental work on passive walking and running was done by McGeer in [17],[18] and [19]. A simple modelisation for running with compliant legs brings the spring-mass model also known as spring-loaded inverted pendulum (SLIP, [6], [20]). The running stability for the SLIP model is examined in [26]. In [23] it is shown that leg segmentation can improve the running stability by using a two-segmented leg. The improvement over the telescopic leg is achieved due to the non-linear relation between leg force and leg length that results from the leg segmentation. The optimal non-linear leg stiffness for a telescopic leg in terms of the Gait Sensitivity Norm [12] is presented in [15].
The research is done in simulation having a single hopping leg. The reduction to a single leg is justified by the fact that in bipedal running only one leg touches the ground at the same time. A symmetric gait of a quadruped (e.g. trot) is similar to bipedal running where each leg supports approximately half the body mass. The simulation is done in Matlab®.
We hope to inherit the characteristics of the simulation model to the legs of the real Cheetah robot.

Arrangement of the Work

In chapter 2 a passive, energy conservative physical model for a telescopic leg and the pantograph leg of the Cheetah robot are presented. The focus is on stabilising mechanisms based on passive dynamics similar to [23]. In chapter 3 a model is presented which aims to achieve stable gaits controlling the pantograph leg. The leg angle can be controlled by a motor at the hip in series with a compliance, similar to [21].

Chapter 2

Energy Conservative System

2.1 SLIP Model

α_0	angle of attack
F_{leg}	leg force
g	gravitational acceleration: 9.81 m/s^2
k_{leg}	leg stiffness
L_0	length of the fully extended leg
L	current leg length
m	body mass
n	number of steps to fall
x, y	coordinates of the centre of mass
x_{td}	x-coordinate at touchdown
$y_{apex,i}$	apex height at stride i
y_{td}	y-coordinate at touchdown

Table 2.1: Parameters for the SLIP Model

Running can be described as a series of flight and stance phases. In [6] and [26] the spring loaded inverted pendulum (SLIP) is used as a physical model. The model is kept very simple: The body is represented by a point mass m, the leg by a massless linear spring of stiffness k_{leg} and length L_0 when fully extended. As the leg is massless, it has no moment of inertia. The leg touches the ground with a constant angle of attack α_0. During the stance phase the leg angle changes naturally with the motion. In the flight phase the angle of attack is reset to α_0. A swing-forward from the leg angle at lift-off to reach again α_0 is not performed, but the angle of attack is reset immediately. Effects of friction or other non-conservative forces are neglected, therefore the system is energy conservative.

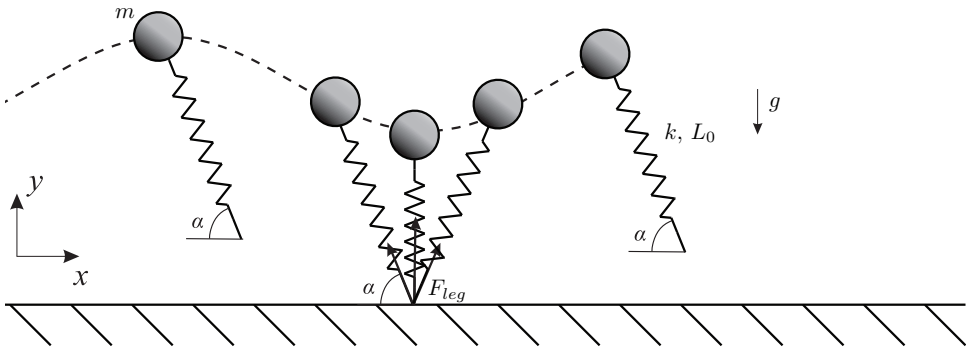

Figure 2.1: The SLIP model

2.1.1 Stance Phase

The leg touches the ground with the angle of attack α_0. During the stance phase the foot is fixed on the ground. The effects of friction, damping or slipping are not taken into account. The only active force besides gravity is the leg force F_{leg}. The equation of motion is given by

$$\begin{pmatrix} m\ddot{x} \\ m\ddot{y} \end{pmatrix} = \begin{pmatrix} -F_{leg} \cdot \cos\alpha \\ F_{leg} \cdot \sin\alpha - mg \end{pmatrix} \tag{2.1.1}$$

with

$$F_{leg} = k_{leg} \cdot (L_0 - L) \tag{2.1.2}$$

where $\vec{F}_{leg} = [F_x, F_y]^{\mathrm{T}}$ directs from the floor contact point to the point mass; the leg angle α is defined by

$$\alpha = \pi - \arccos\left(\frac{x - x_{td}}{\sqrt{(x - x_{td})^2 + y^2}}\right) \tag{2.1.3}$$

with x_{td} the x-coordinate at touchdown.

2.1.2 Flight Phase

During the flight phase the leg has no effect on the system dynamics ($F_{leg} = 0$). Therefore the equations of motion are those of a ballistic flight of a point mass

$$\begin{pmatrix} m\ddot{x} \\ m\ddot{y} \end{pmatrix} = \begin{pmatrix} 0 \\ mg \end{pmatrix}. \tag{2.1.4}$$

2.1.3 Touchdown and Lift-off Conditions

Every stance phase begins with the touchdown of the leg. Touchdown occurs when the mass reaches the touchdown height y_{td} which depends on α_0. This is the case for

$$\text{flight} \rightarrow \text{stance}: \; y \leq L_0 \cdot \sin\alpha_0 = y_{td} \tag{2.1.5}$$

The stance phase ends with lift-off, which occurs when the leg reaches again its initial length L_0.

$$\text{stance} \rightarrow \text{flight: } L > L_0 \tag{2.1.6}$$

where α_0 is the fixed touchdown angle and L_0 the length of the fully extended leg.

2.1.4 System Energy

The state of the running model is defined by the position $[x, y]^{\mathrm{T}}$ and the velocity $\vec{v} = [v_x, v_y]^{\mathrm{T}}$. At the time in the flight phase when $v_y = 0$ (referred to as apex) the system is fully described by x, y_{apex} and v_x. However, on even ground the horizontal position x has no influence on the future system dynamics. Thus the system state is completely described by y_{apex} and v_x. The system energy is given by

$$E_{sys} = \frac{m \cdot \vec{v} \cdot \vec{v}^{\mathrm{T}}}{2} + m \cdot \vec{g} \cdot \vec{h} = const. \tag{2.1.7}$$

at the apex it can be simplified to

$$E_{sys} = \frac{m \cdot v_x^2}{2} + m \cdot g \cdot y_{apex} = const. \tag{2.1.8}$$

As the energy is constant (defined with the initial conditions), the system state is fully described by either v_x or y_{apex}. For the simulation in Matlab® it is indifferent which variable is sampled but for a real-world application the apex height y_{apex} is easier to measure than the velocity v_x. In other works like [23] and [26] also the apex height y_{apex} is tracked.

2.2 Three-Segmented Pantograph Leg

α	angle of attack of the virtual leg
β	redundant angle of attack of the virtual leg $\beta = \pi - \alpha$
η	angle of attack of the pantograph leg
ϕ	leg angle between l_3 and c
γ	leg angle between l_1 and l_2
c_{spring}	stiffness of the spring
h	l_2
d_{14}	normalised distance of the spring attachement
d	current length of the spring
Δd	compression of the spring
Δl	compression of the virtual leg
g	gravitational acceleration: 9.81 m/s^2
i	absolute distance of the spring attachement ($d_{14} \cdot L_0$
j	$l_1 + l_3$
L_0	length of the fully extended leg: 0.16 m
λ_1	normalised length of the first leg segment (thigh/scapula)
λ_2	normalised length of the second leg segment (shank/upper arm)
λ_3	normalised length of the third leg segment (foot/lower arm)
l_1	absolute length of the first leg segment (thigh/scapula)
l_2	absolute length of the second leg segment (shank/upper arm)
l_3	absolute length of the third leg segment (foot/lower arm)
m	mass: 0.5 kg (half the mass of the Cheetah robot)

Table 2.2: Parameters for the Pantograph Leg Model, for an illustration see Fig. 2.2.

The leg of the Cheetah robot is a three-segmented pantograph leg, i.e. the first and the third leg segment are forced parallel. A linear spring is attached between the first and the third segment (see Fig. 2.2). Possible design parameters are the lenghts of the three segments λ_i, the distance d_{14} at which the spring is attatched, as well as the spring stiffness c_{spring} ([29], [28]).

$$L_0 = l_1 + l_2 + l_3 \tag{2.2.1}$$

$$l_i = \lambda_i \cdot L_0 \tag{2.2.2}$$

$$d_{14} \leq \lambda_1 \tag{2.2.3}$$

$$\gamma = \arccos\left(\frac{-c^2 + j^2 + h^2}{2jh}\right) \tag{2.2.4}$$

From angle of attack β of the virtual leg, to the real angle of attack η

$$\phi = \arcsin\left(\lambda_2 \frac{\sin(\gamma)}{L}\right) \tag{2.2.5}$$

$$\eta = \beta - \phi \tag{2.2.6}$$

2.2.1 Virtual Leg

The pantograph leg can be reduced to a virtual leg (dashed line in Fig. 2.2). The virtual leg is a telescopic leg with equivalent properties to the pantograph leg in terms of the leg force. The studies referring to the pantograph leg are applying the reduction to the virtual leg.

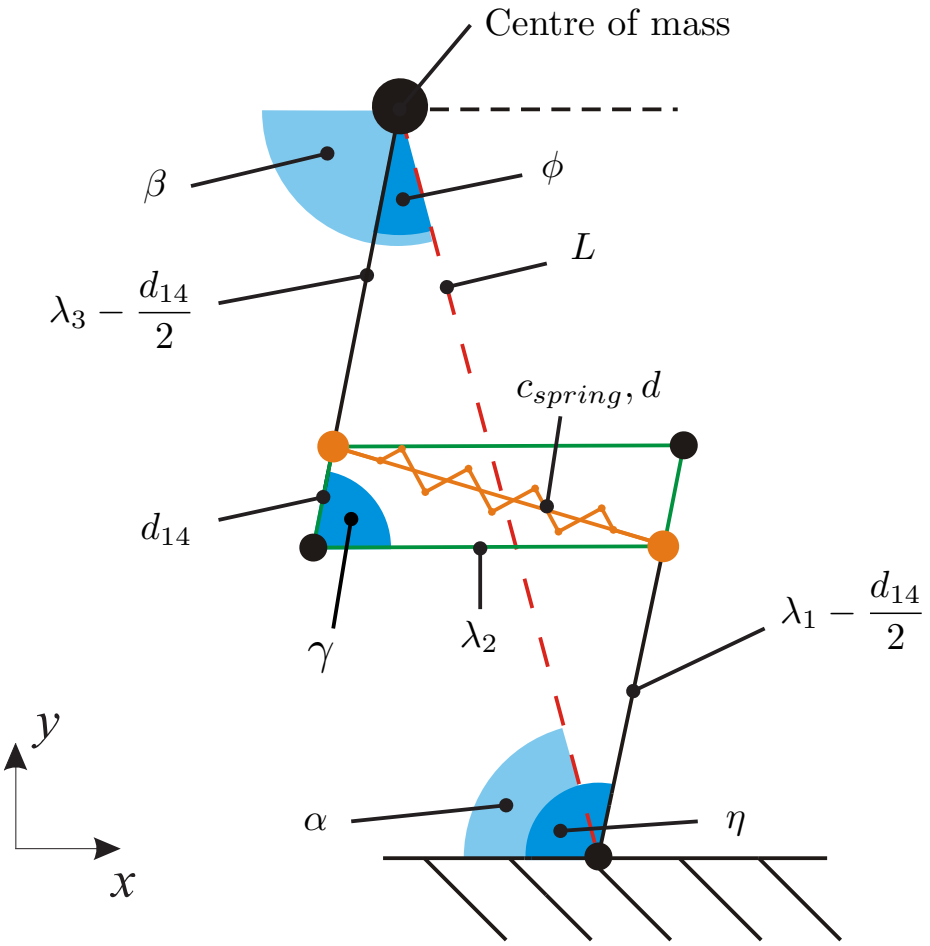

Figure 2.2: The Cheetah's pantograph leg from [28] with the various leg parameters. The dashed line is the virtual single-segmented leg.

2.2.2 Leg Force

The equations of motion Eq. 2.1.1 and Eq. 2.1.4 remain the same except for the leg force F_{leg}. Depending on the choice of the leg parameters the corresponding leg force of the virtual leg can be calculated with Eq. 2.2.7. The force vector $\vec{F}_{leg}$ still points from the ground contact point to the center of mass. Fig. 2.3 shows relation between leg force F_{leg} and leg length (leg compression) for different λ_2 and $d_{14} = 0.1$.

$$\begin{aligned} F_{leg} &= \left(\frac{L}{d}\right)\left(\frac{i}{j}\right) c_{spring}\Delta d \\ F_{leg} &= \left(\frac{1}{d}\right)\left(\frac{i}{j}\right) c_{spring}\Delta d\sqrt{j^2 + h^2 + \frac{j}{i}(d^2 - i^2 - h^2)}. \end{aligned} \tag{2.2.7}$$

In [28] it is shown that the resulting leg stiffness of the virtual leg depends on the choice of λ_2, d_{14} and c_{spring}, but not on the segments λ_1 and λ_3. For simplicity the segments λ_1 and λ_3 are chosen of equal size according to

$$\lambda_1 = \lambda_3 = \frac{1 - \lambda_2}{2}. \tag{2.2.8}$$

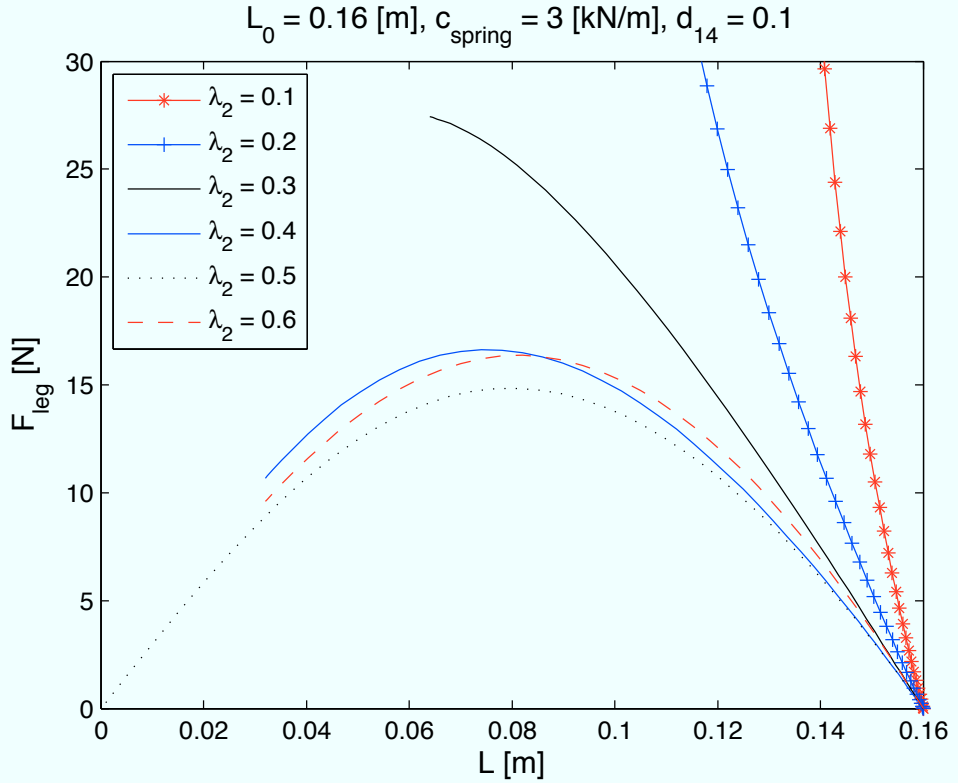

Figure 2.3: The Leg force F_{leg} depending on virtual leg length L, for different λ_2, $d_{14} = 0.1$. For $\lambda_2 < 0.3$ the relation has a progressive shape, for $\lambda_2 = 0.3$ the shape is almost linear and for $\lambda_2 > 0.3$ it is degressive.

Spring Preloading

A possibility to get a different behaviour for F_{leg} than in Fig. 2.3 is to preload the spring. By doing so the leg has no more zero leg force at ground contact, instead the value of F_{leg} at touchdown depends on the preloading. Including an initial displacement Δd_{pre} of the spring, Eq. 2.2.7 becomes

$$F_{leg} = \left(\frac{1}{d}\right)\left(\frac{i}{j}\right) c_{spring}\,(\Delta d + \Delta d_{pre})\sqrt{j^2 + h^2 + \frac{j}{i}(d^2 - i^2 - h^2)}. \qquad (2.2.9)$$

Instead of having a fixed amount of preloading Δd_{pre}, a possibility to have non-zero F_{leg} at touchdown is to land with a leg length $L < L_0$. For example landing with a leg length $L = 0.9 \cdot L_0$ gives the same leg force, like having a preloading of $\Delta d_{pre} = 5.15\%$.

2.2.3 Reference Stiffness

With Eq. 2.2.7 the leg force can be calculated for any given leg length L. To more easily compare different leg stiffness shapes (linear, progressive, degressive) a reference leg stiffness is defined according to [23]. The reference stiffness is defined at 10% leg compression ($\Delta l_{10\%}$), as this is a typical value for the leg compression during running. Based on the corresponding leg force $F_{10\%}(\Delta l_{10\%})$ of the pantographic leg

model, the reference stiffness can be defined as

$$k_{10\%} = \frac{F_{10\%}}{\Delta l_{10\%}} = \frac{9 \cdot i}{d \cdot j} \cdot c_{spring} \cdot \Delta d \tag{2.2.10}$$

or vice-versa to calculate the spring stiffness for a certain $k_{10\%}$

$$c_{spring} = \frac{k_{10\%}}{\Delta d} \cdot \frac{d \cdot j}{9 \cdot i} \tag{2.2.11}$$

with

$$\Delta d = (h + i) - \sqrt{i^2 + h^2 - 2ih\cos(\gamma)}. \tag{2.2.12}$$

This stiffness can be compared for different leg parameters i.e. for different nonlinear leg stiffnesses.

2.2.4 Froude Number

The Froude number gives a dimensionless relation for speed and inertia. In [5] the Froude number for running mammals is calculated using a relation between speed and leg length:

$$Fr = \frac{v_x^2}{g \cdot L_0} \tag{2.2.13}$$

$$v_x = \sqrt{Fr \cdot g \cdot L_0}. \tag{2.2.14}$$

Where v_x is the horizontal velocity, g the gravitational acceleration and L_0 the leg length. According to [5], cats are trotting for Froude numbers of $Fr \approx 1.0$ ($v_x = 1.5$ m/s, $L_0 = 23$ cm). For the Cheetah robot's leg length ($L_0 = 160$ mm) $Fr = 1.0$ corresponds to a speed of $v_x = 1.25$ m/s. Interesting velocities for the stability analysis are therefore arround speeds of $v_x = 1.25$ m/s. The current Cheetah robot's top speed is though $v_x \approx 0.3$ m/s (walking gait patterns). As this is much lower than the desired 1.25 m/s also stable solutions for low speeds are of interest.

2.3 Stability Analysis

In this section two methods for analysing the system stability are presented that were also used in [26] and [23]. The first approach, the steps-to-fall method, examines the ability of the model to generate continuous running by counting the number of successful steps. The second method, the apex return map, examines the behaviour of the system based on a Poincaré map of two subsequent apex heights.

2.3.1 Steps-to-fall Method

In the steps-to-fall method the number of successive steps n is counted for given initial conditions. A simulation run is always startet at apex, the initial conditions are therefore specified by the apex height $y_{apex,0}$ and the horizontal velocity $v_{x,0}$. For given initial conditions and a set of model parameters, the system may

(1) slow down and fall consequently

(2) overrun a step and fall

(3) remain stable in a periodic movement pattern

In case (3) the number of steps to fall is infinite ($n = \infty$). The simulation was stopped when the maximal number of steps ($n = 25$) was reached. In cases (1) and (2) the number of steps until the mass hit the floor were counted. The method identifies potentially stable configurations in a intuitive way. But as the simulation has to stop after a finite number of steps, there is no guarantee that the system will not fall eventually. To check if the solutions are stable for an infinite number of steps the following method, the apex return map is used.

2.3.2 Apex Return Map

In this method, running stability requires the following two conditions:

(1) the solution is periodic with identical apex heights

(2) perturbations in the initial apex height are reduced after one step

A step is defined as the period between two subsequent apexes $y_{apex,i}$ and $y_{apex,i+i}$. The conditions for periodicity and local stability are

$$y^* = y_{apex,i} = y_{apex,i+1} \tag{2.3.1}$$

$$\left| \frac{\partial y_{apex,i+1}}{\partial y_{apex,i}} \right|_{y^*} < 1. \tag{2.3.2}$$

For a given system energy E_{sys}, angle of attack α_0 and leg parameters the apex return map $y_{apex,i+1} = \mathcal{P}(y_{apex,i})$ can be calculated with the equations of motion. The funciton is defined for the possible apex heights $L_0 \sin\alpha_0 \leq y_{apex,i} \leq E_{sys}/mg$. The following paragraph describes the used Poincaré map more in detail.

Poincaré Map

Sampling the state at a discrete event of the gait cycle, defines a Poincaré section ([13], [14]). As it has been shown previously, the apex is a good point in time for sampling as there the system state is defined by the apex height y_{apex}. There is a function known as a Poincaré map $\mathcal{P}$ that describes the evolution from the state at intersection i of the Poincaré section $y_{apex,i}$ to the subsequent intersection $y_{apex,i+1}$

$$y_{apex,i+1} = \mathcal{P}(y_{apex,i}). \tag{2.3.3}$$

The equilibrium state defines a periodic motion that returns to itself upon subsequent intersections, i.e.

$$y^* = \mathcal{P}(y^*). \tag{2.3.4}$$

Linearising the map about the equilibrium point y^* gives,

$$y_{apex,i+1} - y^* = J^* \cdot (y_{apex,i} - y^*) \tag{2.3.5}$$

where J^* is the Jacobian matrix.

$$J^* = \begin{bmatrix} \frac{\partial f_1}{\partial x_1} & \cdots & \frac{\partial f_1}{\partial x_i} \\ \vdots & \ddots & \vdots \\ \frac{\partial f_i}{\partial x_1} & \cdots & \frac{\partial f_i}{\partial x_i} \end{bmatrix}. \tag{2.3.6}$$

The eigenvalues of this matrix are called the Floquet multipliers. The motion is stable when the magnitude of all Floquet multipliers is less than unity.

In our case the Poincaré map has only one dimension, therefore the also one dimensional Jacobian matrix equals its only eigenvalue. The motion is stable, if Eq. 2.3.7 is true

$$J^* = \left| \frac{y_{apex,i+1} - y^*}{y_{apex,i} - y^*} \right| < 1 \tag{2.3.7}$$

where y^* is a stable fixed point. A fixed point is stable if again the Floquet multipliers are less than unity. Here this is the case if

$$J^* = \left| \frac{\partial f(y_{apex,i})}{\partial y_{apex,i}} \right|_{y^*} < 1 \tag{2.3.8}$$

where the derivative can be approximated with e.g.

$$\frac{\partial f(y_{apex,i})}{\partial y_{apex,i}} \approx \frac{f(y^* + h) - f(y^*)}{h} = \frac{f(y^* + h) - y^*}{h}. \tag{2.3.9}$$

Fixed Point Search

To find the fixed points y^* an iterative search is needed. For this purpose Newton's method to find zero crossings is used [2].

$$x_m = x_{m-1} - \frac{F(x_{m-1})}{F'(x_{m-1})}. \tag{2.3.10}$$

In our case we search for points on the diagonal $y = x$. Therefore the problem states as

$$F = f(y_{apex,i}) - y_{apex,i} = y_{apex,i+1} - y_{apex,i} \stackrel{!}{=} 0 \tag{2.3.11}$$

with

$$F' = \frac{\partial F}{\partial y_{apex,i}} = f'(y_{apex,i}) - 1 \tag{2.3.12}$$

where the derivative is approximated with e.g.

$$f'(y_{apex,i}) = \frac{f(y_{apex,i} + h) - f(y_{apex,i})}{h}. \tag{2.3.13}$$

So the problem to be solved by Newton's method is

$$\begin{aligned} y_i^{m+1} &= y_i^m - \frac{f(y_i^m) - y_i^m}{f'(y_i^m) - 1} \\ y_i^{m+1} &= y_i^m - \frac{f(y_i^m) - y_i^m}{\frac{f(y_i^m + h) - f(y_i^m)}{h} - 1} \\ y_i^{m+1} &= y_i^m - \frac{y_{i+1}^m - y_i^m}{\frac{f(y_i^m + h) - f(y_i^m)}{h} - 1}. \end{aligned} \tag{2.3.14}$$

In a Poincaré map for our system there can be up to three fixed points. The Poincaré map with a variable spring constant (Fig. 2.4, $d_{14} = 0.1$, $\lambda_2 = 0.5$) suggests that this is the case only in a small band arround $k_{10\%} \approx 700$N/m (see the slized graph at $k_{10\%} = 700$ N/m in Fig. 2.5). The fixed points are located where the curve crosses the diagonal. For this shape of the Poincaré map only the smallest and biggest fixed point can potentially be stable. The middle fixed point cannot be stable because it crosses the diagonal from the bottom up. As the diagonal has slope = 1 the slope

of the middle fixed point has to be > 1 and therefore the condition in Eq. 2.3.2 is not fulfilled. Apart from the fact that the biggest fixed point is not in the area of interest ($y_{apex,i}$ is almost $2 \cdot L_0$) it is not stable. Although the slope for this third intersection decreases for higher stiffness e.g. the slope at the intersection at $k_{10\%} = 2000$ is still -2 (which is beyond the area of interest for the leg stiffness). Calculating the slope of this intersection for very high leg stiffness suggests that it gets closer to -1 but never becomes stable.
The algorithm detects only a single stable fixed point (if there is any), namely the smallest. There is no guarantee that no other fixed point is stable, but it was never observed that there was more than the one stable fixed point.
The only case where the algorithm was observed to fail to find an existing stable fixed point was, when the stable fixed point was located on a piecewise continuously defined part of the Poincaré map, which was smaller than the distances between the initial guesses for Newton's method.

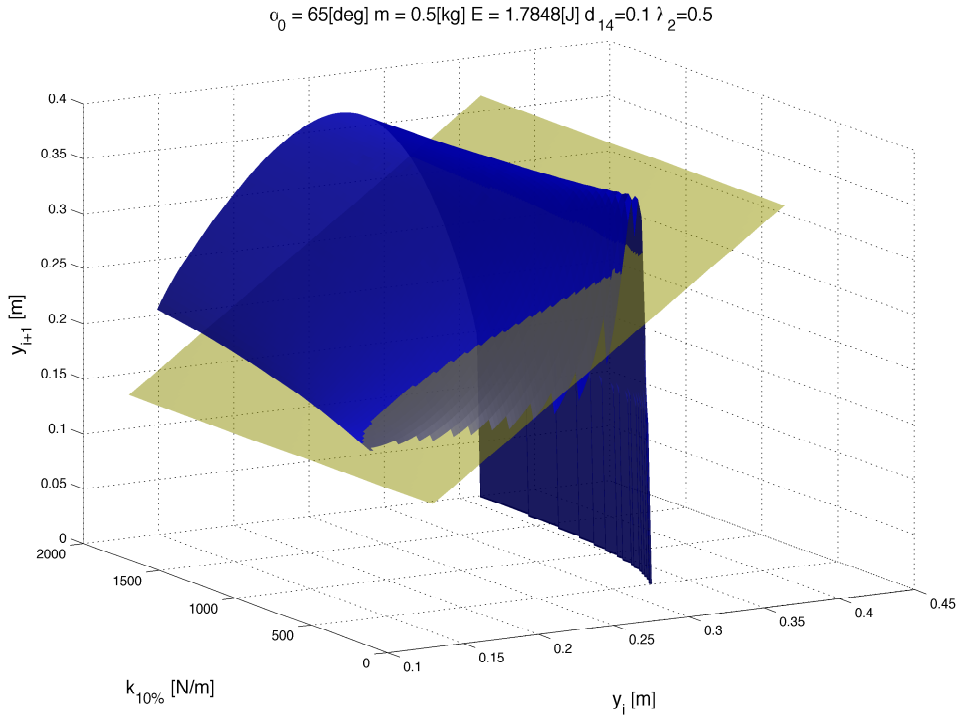

Figure 2.4: Poincaré map with variable spring constant $k_{10\%}$, for the parameters: E = 1.7848 J, $\alpha_0 = 65°$, $m = 0.5$ kg, $L_0 = 0.16$m, $d_{14} = 0.1$ and $\lambda_2 = 0.5$. The inclined plane indicates where $y_{apex,i} = y_{apex,i+1}$. The fixed points are located where the plane crosses the graph. The relevant part of the graph is where the graph crosses the plane three times, as the first intersection is a possibly stable fixed point. A section where there are three intersections is shown in Fig. 2.5.

2.3.3 Example

For the system with the parameters $y_0 = 1$ m, $v_x = 5$ m/s, $m = 80$ kg, $L_0 = 1$ m and $\alpha_0 = 68°$ the corresponding system energy is

$$E_{sys} = mgy_0 + \frac{mv_x^2}{2} = 1784.8[J]. \tag{2.3.15}$$

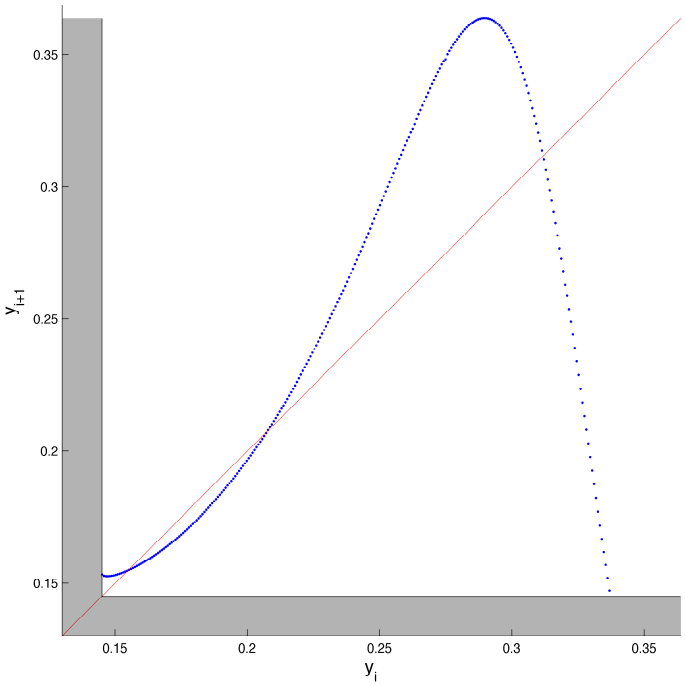

Figure 2.5: Poincaré map of Fig. 2.4 slized at $k_{10\%} = 700$ N/m. The parameters are: E = 1.7848 J, $\alpha_0 = 65°$, $m = 0.5$ kg, $L_0 = 0.16$m, $k_{10\%}$= 700 N/m, $d_{14} = 0.1$, $\lambda_2 = 0.5$

The Poincaré map for these parameters results in the blue graph depicted in Fig. 2.6. The red diagonal indicates where $y_{apex,i} = y_{apex,i+1}$. So the fixed points are located where the blue graph crosses the diagonal. The gray area tags the heights $y_{apex} < L_0 \sin \alpha_0$, which is the minimal lift-off/touchdown height for both $y_{apex,i}$ and $y_{apex,i+1}$. Therefore the graph is not defined in this area. The blue graph crosses the diagonal three times, so there are three fixed points. By looking at the graph in Fig. 2.6, one can clearly see that the slope of the graph at the fixed points at about $y_{apex,i} \approx 2$ and $y_{apex,i} \approx 1.35$ is > 1, whereas at the fixed point at about $y \approx 0.95$ the slope is < 1. According to Eq. 2.3.8 only the latter fixed point is stable. With Eq. 2.3.7 it can be determined whether the configuration is stable. Fig. 2.7 shows the Poincaré map for a case, where the steps to fall method suggests that the configuration is stable. But as the blue line never crosses the red line, there are no stable fixed points. Because the apex hight increases very slowly the system is stable for the 25 steps tested in the steps to fall method, but it will in this case become unstable after 63 steps (Fig. 2.8).

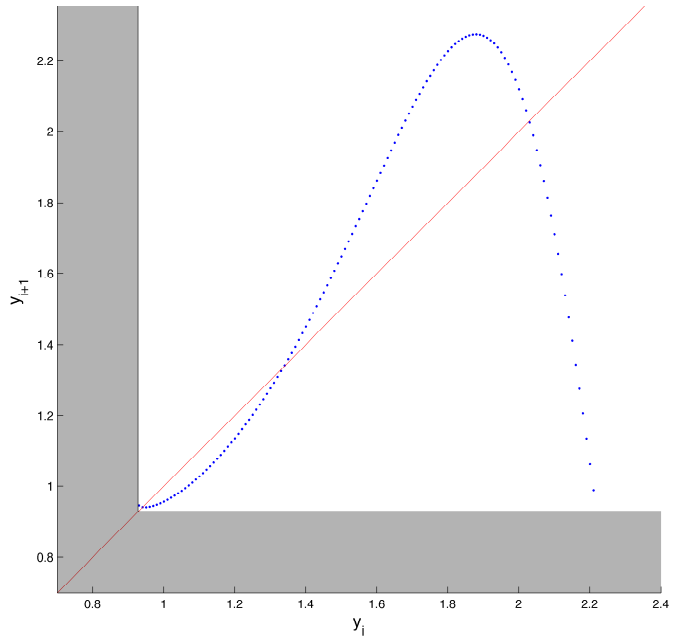

Figure 2.6: Poincaré Map for Parameters: $E_{sys} = 1784.8$ J, $\alpha_0 = 68°$, $m = 80$ kg, $L_0 = 1$ m and $k_{leg} = 20$ kN/m.

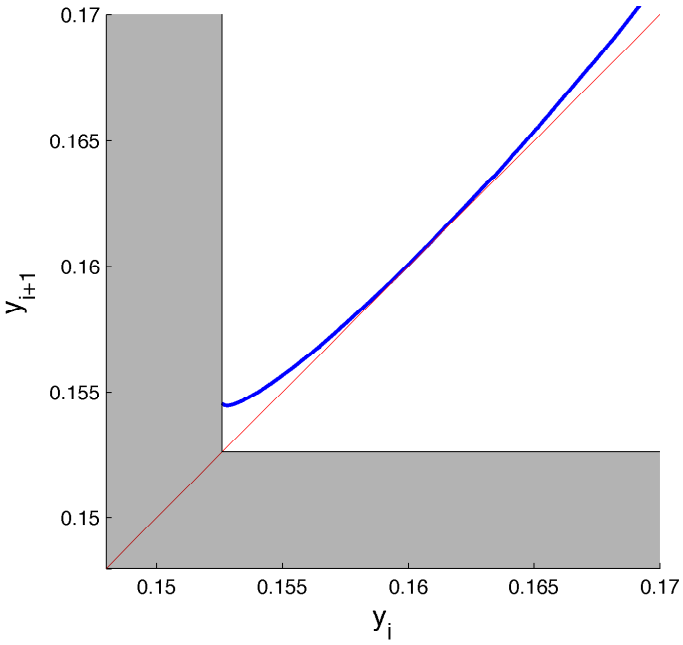

Figure 2.7: Poincaré Map for the configuration: $E_{sys} = 1.3473$ J, $\alpha_0 = 72.5°$, $m = 0.5$ kg, $L_0 = 0.16$ m, $k_{leg} = 9.6$ kN/m and $k_{10\%} = 4.37$ kN/m. The Poincaré map never crosses the diagonal where $y_{apex,i} = y_{apex,i+1}$, thus there are no stable fixed points.

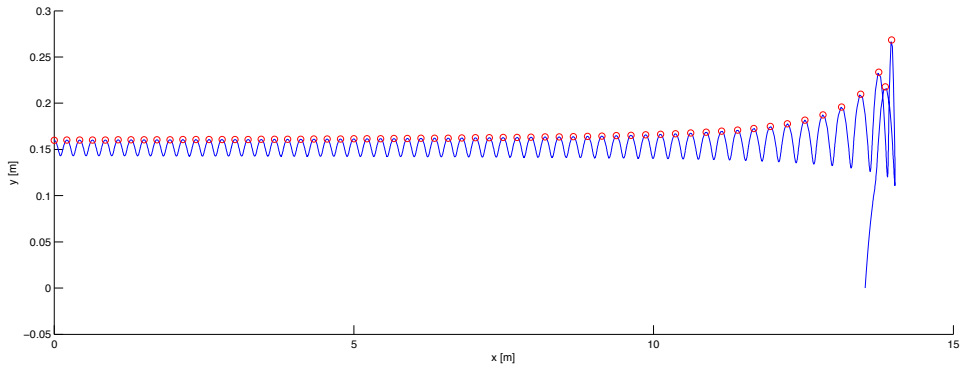

Figure 2.8: Trajectory of the point mass with indicated apexes (red circles) for the parameters: $v_0 = 1.5$ m/s, $y_0 = 0.16$m, $\alpha_0 = 72.5°$, $m = 0.5$ kg, $L_0 = 0.16$ m, $k_{leg} = 9.6$ kN/m and $k_{10\%} = 4.37$ kN/m. The system seems stable for a couple of steps, but finally becomes unstable after 63 steps.

2.4 Results Telescopic Leg

To verify the valitdity of the simulation model, the results obtained in [26] were reconstructed. Stable running requires a proper adjustment of leg stiffness k_{leg}, angle of attack α_0 and running speed $v_{x,0}$. In Fig. 2.9 either the horizontal velocity v_x, the angle of attack α_0 or the spring stiffness k is held constant. Comparing Fig. 2.9 and Fig. 2.10 suggests that the simulation used in this work and the simulation in [26] lead to equivalent results.

Simulation Setup

In [26] parameters which are similar to the human leg are used. The simulation is started at the apex with initial conditions $x_0 = 0$, $y_0 = L_0$, $v_{x,0} =$ const. and $v_{y,0} = 0$. Model parameters are the leg length L_0, the body mass m, the angle of attack α_0 and the leg stiffness k_{leg}. Typical values for the human leg used in [26] are $L_0 = 1$ m, $m = 80$ kg, $\alpha_0 = 68°$ and $k_{leg} = 20$ kN/m.
The simulation tool is Matlab 7.9® with the *ode*45() solver.

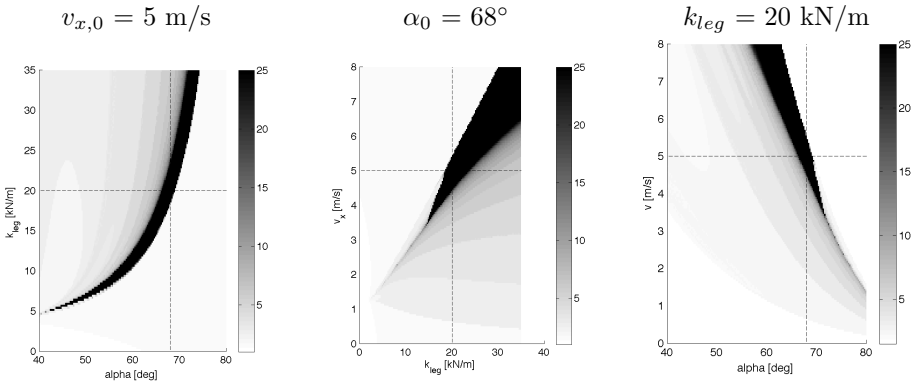

(a) (b) (c)

Figure 2.9: In each diagram one parameter is kept constant: (a) $v_{x,0} = 5$ m/s, (b) $\alpha_0 = 68°$, (c) $k = 20$ kN/m. The integration stopped if the point mass fell onto the ground ($y = 0$) or the maximal number of steps was reached ($n = 25$, grayscale on the right). The black areas in the diagrams ($n = 25$) indicate potentially stable parameter configurations.

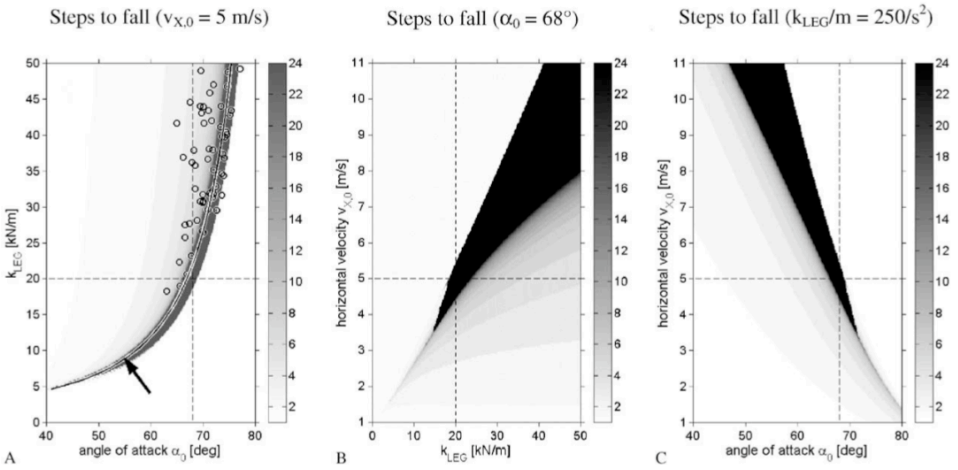

Figure 2.10: Copied from [26] p. 652. The integration stopped if the point mass fell onto the ground or the step number n exceeded 24. In (A) the initial horizontal speed $v_{x,0}$ is kept constant at 5 m/s, in (B) the angle of attack is kept at 68° and in (C) the leg stiffness is kept constant at 20 kN/m. The circles in A denote experimental data for running at 4.6 ± 0.5 m/s. The arrow points to a solid line described by a function with $k_{leg} \cdot (1 - \sin \alpha_0)$.

2.5 Results Pantograph Leg

2.5.1 Choice of the Parameters λ_2 and d_{14}

In this section the effect of different parameter choices of λ_2 and d_{14} is investigated. In Fig. 2.11 J-shape-plots (k_{leg} versus α_0) for different leg parameter choices are shown for the same initial horizontal velocity $v_{x,0} = 2$ m/s. The stability was tested with the apex return map. The plots for other initial horizontal velocities and different d_{14} for both the steps-to-fall method and the apex return map are shown in Appendix A.1 and Appendix A.2 respectively. For the low velocities the steps-to-fall method suggests hardly any stable configurations. The apex return map confirms that there are no stable solutions for the horizontal speed of $v_{x,0} = 1$ m/s. For $v_{x,0} = 1.25$ m/s the steps-to-fall method gives a better defined J-shape. But again the apex return map shows that there are no stable configurations. For higher speeds the J-shape is well defined for some configurations. The apex return map shows that the velocity $v_x = 1.5$ m/s is about the limiting speed for stable solutions. At a horizontal speed of $v_{x,0} = 2$ m/s (Fig. 2.11) the influence of the choice of the parameter λ_2 can be well observed. In the first row the stable solutions for the pantograph leg are plotted as black areas. For comparison the stable areas for the SLIP model are plotted in grey. There are clearly more stable solutions for $\lambda_2 = 0.3$ and $\lambda_2 = 0.5$ than for $\lambda_2 = 0.1$. The difference between $\lambda_2 = 0.3$ and $\lambda_2 = 0.5$ is rather small. The J-shape for $\lambda_2 = 0.5$ is though more bent and goes to lower angles of attack than $\lambda_2 = 0.3$. The shape of $\lambda_2 = 0.5$ is more desirable because thanks to the bent curve a wider range of angles of attack are stable for a particular leg stiffness.
According to [23] a degressive leg stiffness curve gives the best running stability. As the best running stability is observed for $\lambda_2 = [0.4, 0.5, 0.6]$ and $d_{14} = 0.1$, which have degressive stiffness curves (see Fig. 2.3), a similar statement can be made. But it has to be added that for these experiments the leg compression has values where the stiffness curve is approximately linear (see Fig. 2.11 in the second row), whereas in [23] the stiffness curves are highly non-linear. On the other hand it can clearly be stated that a largely progressive stiffness curve (as for $\lambda_2 = 0.1$) is a disadvantage for stable running.
Increasing d_{14} leads to smaller regions of stability. For large values of d_{14} the best choices for λ_2 are not feasible because the following geometrical constraint needs to be fulfilled

$$d_{14} \overset{!}{\leq} \lambda_1 = \frac{1 - \lambda_2}{2}. \tag{2.5.1}$$

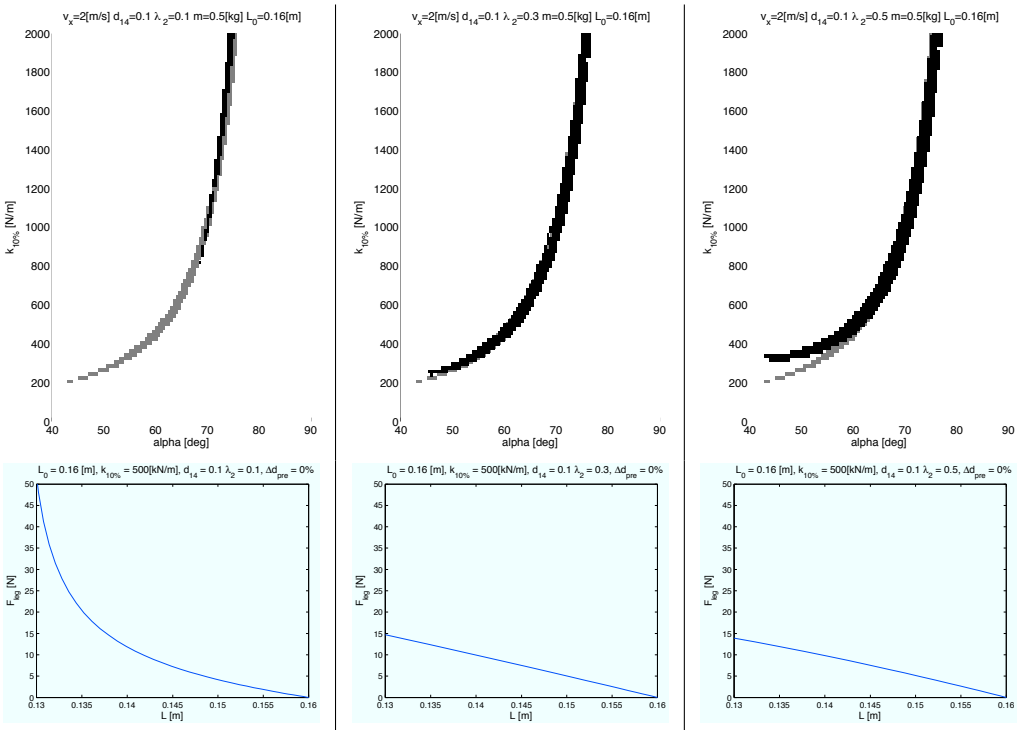

Figure 2.11: The first row shows the stability plots for $\lambda_2 = 0.1$, $\lambda_2 = 0.3$ and $\lambda_2 = 0.5$ tested with the apex return map. The black areas are the stable solutions for the pantograph leg. For comparison the stable area for the linear SLIP model is plotted in grey. The second row shows the leg force for a relevant range of the virtual leg length L. For $\lambda_2 = 0.1$ which has a progressive shape for the leg force, the stable area is drastically decreased. For $\lambda_2 = 0.3$ the area of stability is hardly changed as the leg force has practically a linear shape. For $\lambda_2 = 0.5$ the curve is slightly bent upwards for low angles of attack and low leg stiffness. This is desirable as for a given leg stiffness stable running is possible in a larger band of angles of attack.

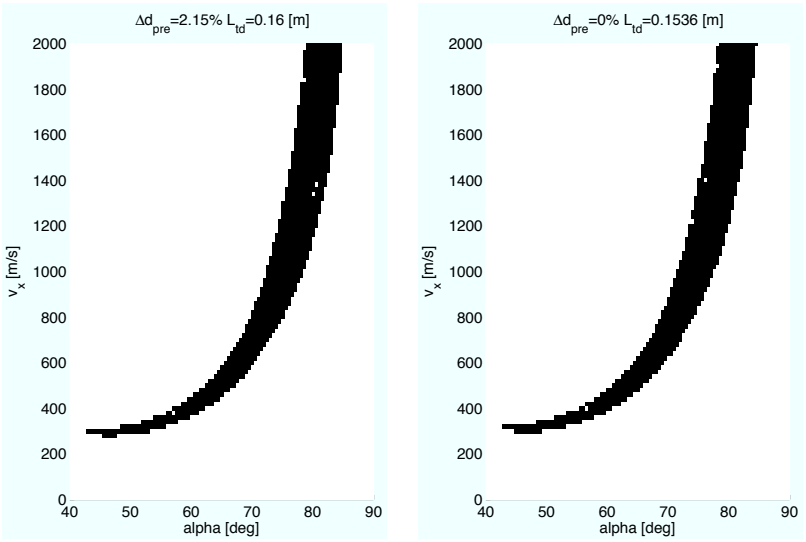

(a) (b)

Figure 2.12: (a) stable areas for a preload of $\Delta d_{pre} = 2.15\%$ (b) the corresponding plot for a precompressed leg at touchdown $L_{td} = 0.96L_0$. The stable areas are almost identical because landing with a leg length $L < L_0$ has practically the same effect as preloading the spring. The stability was tested with the apex return map.

2.5.2 Spring Preloading

In this section the influence of preloading the spring on the system stability is examined. Fig. 2.13 shows the stable regions for preloadings of $\Delta d_{pre} = 0\%$, $\Delta d_{pre} = 2\%$ and $\Delta d_{pre} = 10\%$ of the maximal spring length. The stability was tested with the apex return map. In the first row the stable solutions for the pantograph leg are plotted as black areas. For comparison the stable areas for the SLIP model are plotted in grey. The second row of Fig. 2.13 shows the leg force depending on the leg length L. The plots for other initial horizontal velocities and different Δd_{pre} for both the steps-to-fall method and the apex return map are shown in Appendix A.3 and Appendix A.4 respectively.
By preloading the spring, the stable area is significantly increased but shifted. For a spring without preload there were no stable solutions for the horizontal initial speed $v_{x,0} = 1$ m/s, whereas already with a preloading of $\Delta d_{pre} = 2\%$ stable configurations are found at this speed. For high preloading the area of stability is shifted to higher angles attack, which is a similar effect as increasing the spring stiffness.

Manners of Preloading

Instead of having a fixed amount of preloading Δd_{pre}, it is also possible to land with a leg length $L < L_0$. The resulting plot for a preload of $\Delta d_{pre} = 2.15\%$ is shown in Fig. 2.12 (a) and the corresponding plot for a precompressed leg at touchdown $L_{td} = 0.96L_0$ is shown in Fig. 2.12 (b). Comparing Fig. 2.12 (a) and Fig. 2.12 (b) confirms that the two manners of preloading lead to very similar running stability.

Leg Force

Without preloading the leg force F_{leg} is zero at touchdown. When the spring is preloaded, F_{leg} jumps immediately to a value depending on the amount of

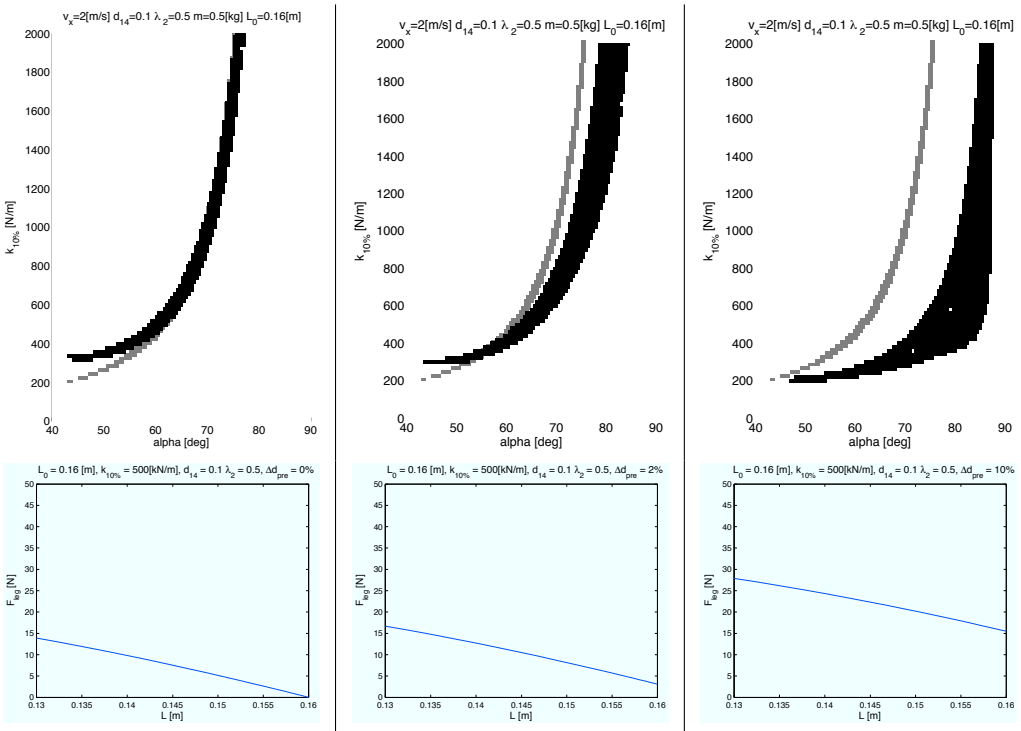

$\Delta d_{pre} = 0\%$ $\Delta d_{pre} = 2\%$ $\Delta d_{pre} = 10\%$

Figure 2.13: The first row shows the stability plots for $\Delta d_{pre} = 0\%$, $\Delta d_{pre} = 2\%$, $\Delta d_{pre} = 10\%$ and $\lambda_2 = 0.5$ tested with the apex return map. The black areas are the stable solutions for the pantograph leg. For comparison the stable area for the not preloaded SLIP model is plotted in grey. The area of stability is increasing with the amount of preloading. Further the area is shifted to higher angles of attack and slightly bent.

preloading. The stance phase gets shorter with increasing preloading, since the peak of the leg force is reached in less time. Fig. 2.14 shows the leg forces F_x and F_y, as well as the virtual leg length L during a stance phase in steady-state.

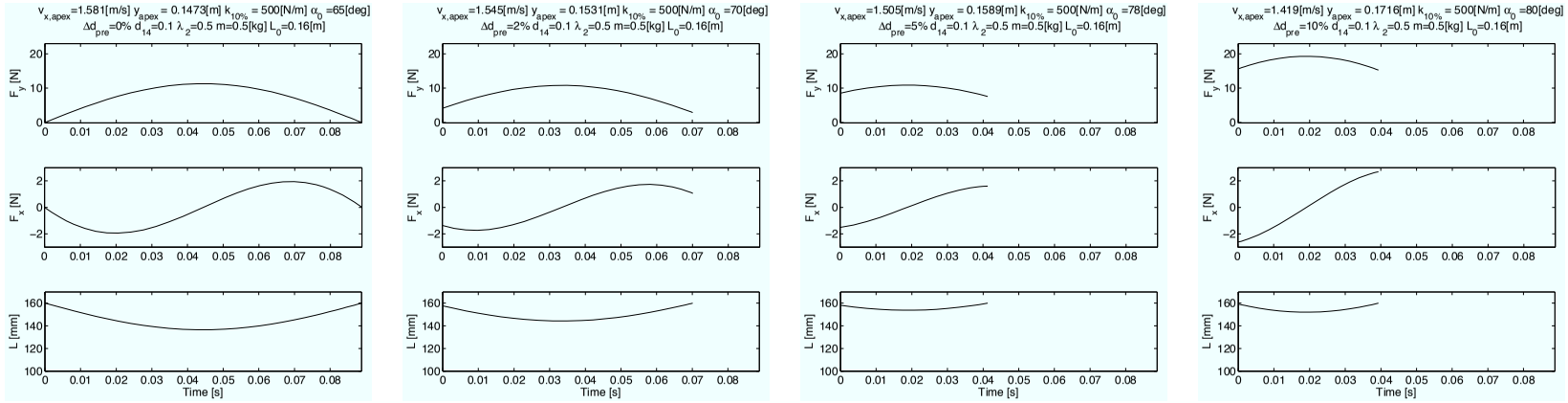

$\Delta d_{pre} = 0\%$ $\Delta d_{pre} = 2\%$ $\Delta d_{pre} = 5\%$ $\Delta d_{pre} = 10\%$

Figure 2.14: F_y, F_x and virtual leg length L for $k_{10\%} = 500$ N/m ($c_{spring} = 4843$ N/m) and different amounts of preloading during one stance phase in steady-state. For a preloaded spring the leg force at touchdown is non-zero. The duration of the stance phase decreases with the amount of spring preloading.

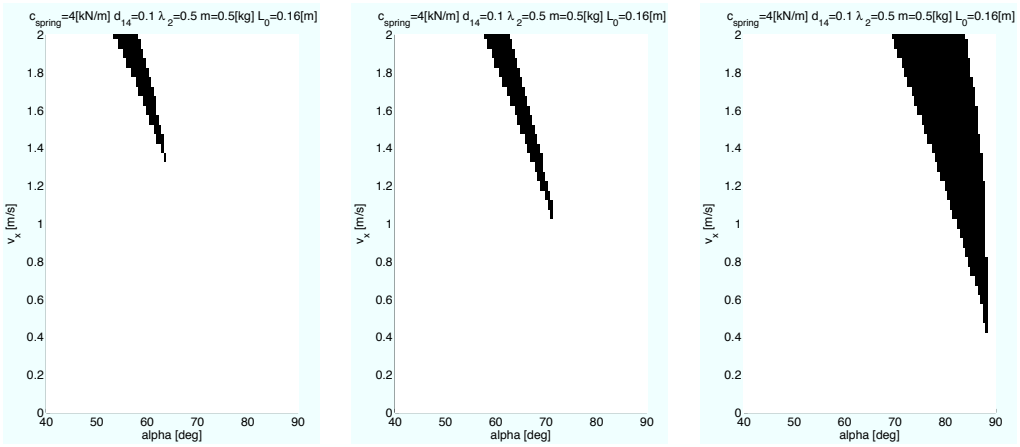

$\Delta d_{pre} = 0\%$ $\Delta d_{pre} = 2\%$ $\Delta d_{pre} = 10\%$

Figure 2.15: The black area indicates the stable areas for $\Delta d_{pre} = 0\%$, $\Delta d_{pre} = 2\%$ and $\Delta d_{pre} = 10\%$ tested with the apex return map. The spring stiffness is constant at $c_{spring} = 4000$ N/m. The initial horizontal speed $v_{x,0}$ and the angle of attack is variated. The minimal velocity which still achieves a stable gait decreases with the amount of spring preloading.

Minimal Speed

There is a minimal speed that still allows stable running. By preloading the spring this speed can be decreased. Fig. 2.15 shows the stable areas for different preloadings for varying speed and angle of attack but constant spring stiffness $c_{spring} = 4$ kN/m. The minimal speed without preload is at 1.3 m/s, whereas for a preload of $\Delta d_{pre} = 2\%$ the minimal speed is at 1 m/s. With a preload of $\Delta d_{pre} = 10\%$ stable running patterns are possible down to a speed of 0.4 m/s. The stable solutions are though shifted to high angles of attack, which is not desirable for the real robot.

Chapter 3

Controlled System

α_0	angle of attack (virtual leg)
α_{leg}	current virtual leg angle
α_{motor}	angle given by the motor (virtual leg)
η_0	angle of attack (pantograph leg)
η_{motor}	angle given by the motor (pantograph leg)
d_{14}	normalised distance of the spring attachement: 0.1
d_{rot}	damping constant between motor and leg
k_{rot}	spring constant between motor and leg
L	current length of the virtual leg
L_{flight}	desired leg length during flight (virtual leg)
L_{lo}	leg length at lift-off (virtual leg)
L_{td}	leg length at touchdown (virtual leg)
λ_2	normalised length of the second leg segment (shank/upper arm): 0.5
m_{leg}	leg mass: 0.02 kg
m	total mass: 0.5 kg
T_{flight}	duration of one flight phase
T_{stance}	duration of one stance phase

Table 3.1: Parameters for the Controlled Pantograph Leg Model

In a real-world application the assumption that there are no energy losses is not valid. On the actual robot the leg is attached to a motor to move the leg. Energy is added to the system by the motor and lost due to dissipative forces (friction, damping). Therefore the assumption of energy conservation is discarded in this chapter and a strategy is presented how energy can be actively added and removed.

3.1 Motor/Spring/Damper

Ideally the motor would make the leg perform the same trajectory as if running passively (i.e. as in the energy conservative system). This means the motor should exactly follow the leg angle during passive running. To do so the leg trajectory has to be known a priori, which is hardly the case in a real-world application. To deal with this, the pantograph leg is connected in series with a torsional spring (Fig. 3.1). Instead of forcing the leg to the motor angle, a torque is induced, which depends on the difference between the motor angle and the actual leg angle (Eq. 3.1.1). This allows the leg to follow the trajectory given by the motor in a more passive way.

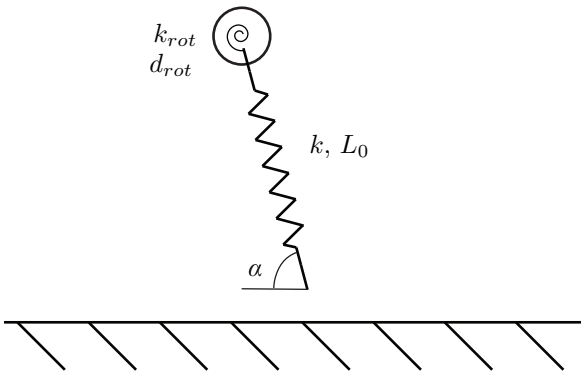

Figure 3.1: In the controlled model the leg is connected in series with a torsional spring with stiffness k_{rot} and damping coefficient d_{rot}.

$$M_{rot} = \Delta\alpha \cdot k_{rot} \tag{3.1.1}$$
$$\Delta\alpha = \alpha_{leg} - \alpha_{motor} \tag{3.1.2}$$

where M_{rot} is the resulting torque, α_{leg} the leg angle, α_{motor} the motor angle and k_{rot} the stiffness of the torsional spring.
In the previous chapter the leg had a constant angle of attack α_0 which was reset externally after lift-off. In this model, the leg has to swing-forward to the desired angle of attack during flight. A perfect spring tends to overshoot such that a swing-forward to a desired angle of attack is almost impossible. Therefore a damping coefficient d_{rot} is assumed.

3.1.1 Choice of the Spring Stiffness k_{rot}

For the spring stiffness k_{rot} the following relations are given

$$k_{rot} = 0 \quad \rightarrow \quad \text{entirely passive running} \tag{3.1.3}$$
$$k_{rot} = \infty \quad \rightarrow \quad \text{perfect motor angle following.} \tag{3.1.4}$$

The spring stiffness k_{rot} has to be chosen as small as possible, but large enough to allow leg swing-forward during the flight phase. As the leg angle for stable passive running is not a priori known and therefore not available as motor command, the spring stiffness has to be chosen as small as possible to not disturbe the passive running. Though it cannot be chosen zero, as the leg swing-forward is no passive movement and has to be enforced by the motor.
The damping coefficient d_{rot} has to be chosen so that the overshooting is manageable, but in a way that the drag allows still a swing-forward during flight. For the experiments in section 3.4 the value of the damping coefficient d_{rot} was set to a value according to [17] ($d_{rot} = 0.01$ Ns/rad).

3.1.2 Equations of Motion

In the previous chapter the system had two degrees of freedom during both the flight and the stance phase. This was the case because the angular orientation of the leg during flight was set to a constant value α_0. In this model the system has

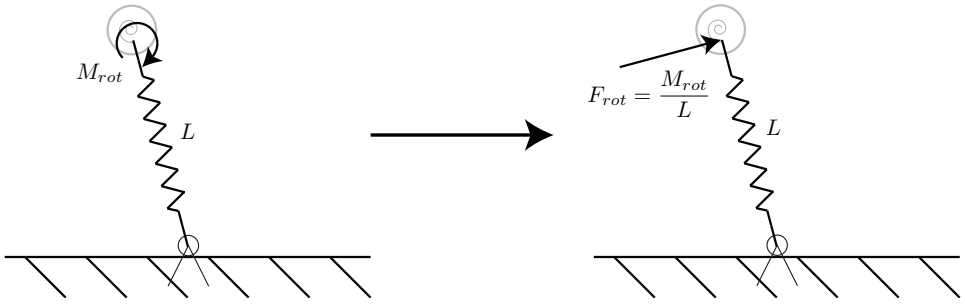

Figure 3.2: The moment induced by the rotational spring can be converted to an equivalent force.

still two degrees of freedom in the stance phase but three degrees of freedom in the flight phase because now the angular orientation is controllable.

Flight Phase

The swing-forward of the leg is performed during the flight phase. In the previous study the leg was massless and had therefore no moment of inertia. To model a physically realistic swing-forward, the leg has to be attributed a moment of inertia. The current Cheetah robot's leg has a mass of $m_{leg} = 0.02$ kg (see [24]). According to [1] the moment of inertia for a rod of length L and mass m_{leg} rotating around its end is

$$I_{leg} = \frac{m_{leg} L^2}{3}. \tag{3.1.5}$$

The equations of motion for flight take the following form

$$\begin{aligned} m\ddot{x} &= 0 \\ m\ddot{y} &= -mg \\ I_{leg}\ddot{\alpha} &= (M_{spring,rot} - M_{damp,rot}) \end{aligned} \tag{3.1.6}$$

with

$$\begin{aligned} M_{spring,rot} &= k_{rot}\Delta\alpha \\ &= k_{rot}(\alpha_{motor} - \alpha_{leg}) \qquad (3.1.7) \\ M_{damp,rot} &= d_{rot}\dot{\alpha}_{leg} \qquad (3.1.8) \end{aligned}$$

Stance Phase

The equations of motion of the stance phase receive additional force terms for the spring and the damper

$$\begin{aligned} m\ddot{x} &= -F_{leg}\cos\alpha_{leg} + (F_{spring,rot} - F_{damp,rot})\sin(\alpha_{leg} + \frac{\pi}{2}) \qquad (3.1.9) \\ m\ddot{y} &= F_{leg}\sin\alpha_{leg} + (F_{spring,rot} - F_{damp,rot})\cos(\alpha_{leg} + \frac{\pi}{2}) - mg. \end{aligned}$$

The forces $F_{spring,rot}$ and $F_{damp,rot}$ result from the torsion, which is converted to a force:

$$\begin{aligned} F_{spring,rot} &= \frac{M_{spring,rot}}{L} \\ &= \frac{k_{rot}\Delta\alpha}{L} \\ &= \frac{k_{rot}(\alpha_{motor} - \alpha_{leg})}{L} \end{aligned} \tag{3.1.10}$$

$$\begin{aligned} F_{damp,rot} &= \frac{M_{damp,rot}}{L} \\ &= \frac{d_{rot}\dot{\alpha}_{leg}}{L}. \end{aligned} \tag{3.1.11}$$

3.2 Swing-Forward Steering

3.2.1 Leg Length

The leg length during the stance phase is not controlled, loading and releasing the spring is done passively. In the flight phase the leg swing-forward has to be performed. To ensure foot clearance in the flight phase the leg is retracted in a sinusoidal shape. As the duration of the flight phase T_{flight} is not a priori known but predicted (see section 3.2.3), the desired leg length at touchdown L_{td} is planned to be reached early. The desired leg length over time is

$$L_{flight} = \begin{cases} -\Delta L_{ret}\sin(\frac{t\pi}{T_{sb}}) + L_{td} & \text{if } t \leq T_{sb} \\ L_{td} & \text{if } t > T_{sb} \end{cases} \tag{3.2.1}$$

where ΔL_{ret} is the maximal leg retraction during swing-forward (e.g $\Delta L_{ret} = 0.2L_0$), $T_{sb} \leq T_{flight}$ is the time for swing back and L_{td} the touchdown leg length. The resulting curve for one flight phase is shown in Fig. 3.3 (a).

3.2.2 Leg Angle

The angle of the virtual leg changes linearly over time

$$\alpha_{flight} = \begin{cases} \frac{t(2\alpha_0 - \pi)}{T_{sb}} + \pi - \alpha_0 & \text{if } t \leq T_{sb} \\ \alpha_0 & \text{if } t > T_{sb} \end{cases} \tag{3.2.2}$$

where α_0 is the desired angle of attack and T_{sb} the time for swing-forward. The corresponding angle for the pantograph leg can be calculated using Eq. 2.2.1 to Eq. 2.2.6. The resulting curves are shown in Fig. 3.3 (b).

3.2.3 Predicting T_{stance} and T_{flight}

Two different methods were tested to predict the duration of the subsequent stance phase and flight phase (T_{stance} and T_{flight}). One method uses the last value as a guess and the other the algorithm described in [4]. The latter uses simplified equations of motion to predict the values of T_{stance} and T_{flight}. The used equations are valid under the assumption that the system is in steady-state and that the spring is not preloaded, which is too restrictive.
The other approach is to predict the values of T_{flight} and T_{stance} by measuring the values in the step i and using them as a guess for the step $i + 1$. This has the advantage that the system state does not have to be known. Further there are no

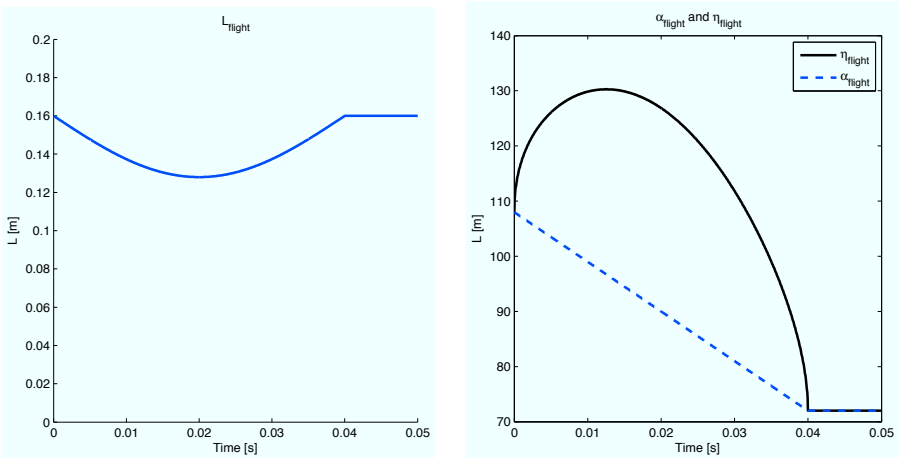

(a) (b)

Figure 3.3: (a) The desired leg length L_{flight} during one flight phase, (b) the desired leg angle $\eta_{motor,flight}$ during one flight phase (solid) and the corresponding leg angle $\alpha_{motor,flight}$ of the virtual leg (dashed).

assumptions necessary that the system has to be in steady-state and that the spring is not preloaded. Therefore finally this approach is used.

3.3 Energy Control

To achieve a stable gait e.g. at a constant velocity, the system energy has to be controllable. The system energy is composed of the potential and kinetic energy

$$E = \frac{m \cdot v^2}{2} + m \cdot g \cdot h. \tag{3.3.1}$$

At the apex the energy is therefore

$$E_{apex} = \frac{m \cdot v_{x,apex}^2}{2} + m \cdot g \cdot y_{apex}. \tag{3.3.2}$$

One tested control strategy was to adapt the angle of attack to get a desired speed. But by only controlling the velocity, the apex height might in- or decrease arbitrarily. To control the system and thus its energy both the velocity and the apex height have to be taken into account.
There are different possibilities to add or remove energy from the system. During stance energy is added and taken from the system by the spring-damper between motor and leg. Namely the spring adds energy to the system and the damper takes energy. If the motor angle matches exactly the passive trajectory of the leg, the spring has no influence and no energy is added. As this is the desired behaviour of the motor, the leg angle during stance is not an option to control the systems energy.
In the energy conservative system, the spring accomodates the ground reaction force and restores it fully to the system until lift-off. In reality the floor acts as a damper and absorbs some of the energy. The floor damping is a given property and therefore not an option to control the system energy.
The chosen strategy to control the system energy actively is to control the leg length at touchdown and lift-off. Energy can be added to the system by having a more compressed leg at touchdown than at lift-off. Vice versa energy can be taken from

the system by having a less compressed leg at touchdown than at lift-off. Like this the controller can add or remove energy by controlling only one parameter. If $L_{lo} < L_{td}$ energy is taken from the system, as not all of the energy stored in the spring is released. If $L_{lo} > L_{td}$ energy is added to the system, as more energy is released as stored during stance. The leg length at lift-off L_{lo} is controlled using a PID controller. The desired angle of attack is set to a constant value, which was found to be stable for the purely passive running in chapter 2.

3.3.1 Controller

K_p	0.05
K_i	0.01
K_d	0.05

Table 3.2: Controller Parameters

The controller which is used is a PID controller (Eq. 3.3.3) with the parameters listed in Tab. 3.2

$$u(t) = K_p e(t) + K_i \int_0^t e(\tau)\, d\tau + K_d \frac{d}{dt} e(t). \tag{3.3.3}$$

Where $e(t)$ is the error and $u(t)$ the controller output. The error is defined as the difference between the desired system energy and the actual system energy (Eq. 3.3.2). The output is the leg length at lift-off L_{lo}. The output is limited to a value about $L_{lo,min} = 0.9L_0$ to avoid very low leg lengths at lift-off, which might lead to instability.

3.4 Results Controlled System

3.4.1 Step

α_0	70°
d_{14}	0.1
d_{rot}	0.01 Ns/rad
k_{rot}	1 N/rad
L_{td}	0.96 L_0 = 0.1536 m $\hat{=}\Delta d_{pre}$ = 2.15%
λ_2	0.5
m_{leg}	0.02 kg
m	total mass: 0.5 kg
$v_{x,0}$	1 m/s
y_0	0.155 m

Table 3.3: Parameters used for the step study

The aim of this section is to study how the system responds to unpredicted changes in the floor altitude. After a certain distance, when the system has reached a steady-state, the floor changes its altitude. For the parameter choice and initial conditions listed in Tab. 3.3 and for the control strategy described in section 3.3, the system was able to handle steps of 1.5 cm either up or down. That is about 10% of the leg length, which would correspond to a step of 10 cm for a human ($L_0 \approx 1$ m). Fig. 3.4 shows the trajectory for a step of -1.5 cm down at x = 5 m and a step up of +1.5 cm at x = 10 m. For the step down the system needs less steps to reach a steady-state than for the step up (Fig. 3.5). In fact the system was observed to handle a step down of -3 cm, whereas the maximal step up to overcome was +1.5 cm.

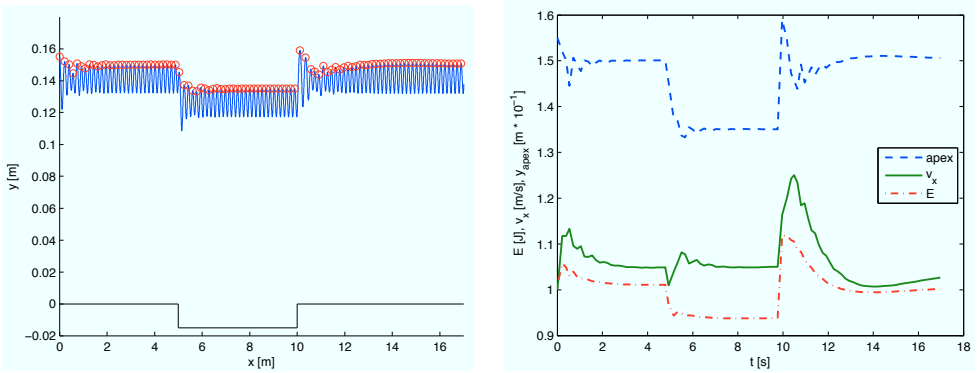

(a) (b)

Figure 3.4: There is a step down of -1.5 cm at x = 5 m and up again at x = 10 m. (a) shows the trajectory of the centre of mass with the apexes indicated with circles, a magnification of the trajectory for the steps is shown in Fig. 3.5. (b) shows the developing of the system energy E_{sys}, the apex height y_{apex} and the horizonatal velocity $v_{x,apex}$.

3.4.2 Energy Measurement Error Estimation

To have a knowledge about the system energy, y_{apex} and $v_{x,apex}$ (or the state at another point in time) have to be known. For an immediate measure exteroceptive

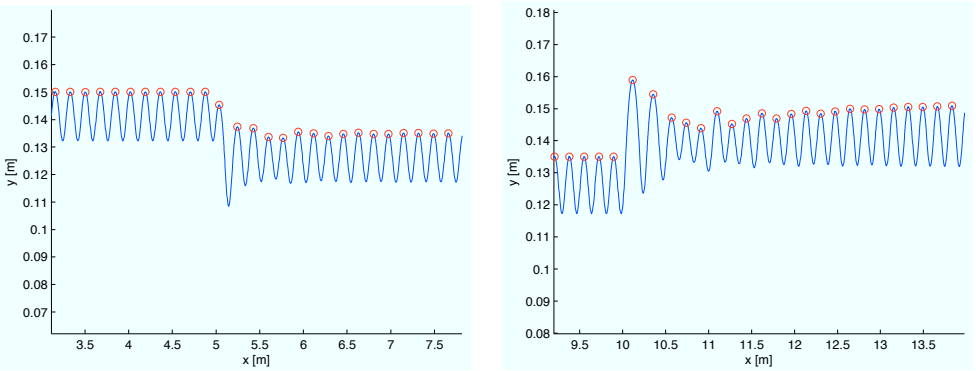

(a) (b)

Figure 3.5: The behaviour of the system for (a) a step down of -1.5 cm at $x = 5$ m and (b) for a step up of +1.5 cm at x =10 m

sensors would be necessary. It is though desirable to use proprioceptive sensors to keep track of the system state. One possibility is to integrate the forces over time to get the speed. The necessary equipement to do so are a touch sensor to sense floor contact and a potentiometer for each leg angle η and γ. The potentiometer which is intended to be used on the real robot has an absolute linear error of $\pm 3\%$ (see [3]). The leg force depending on the leg angle γ can be computed using the following relationships:

$$\begin{aligned} L(\gamma) &= \sqrt{j^2 + h^2 - 2jh\cos\gamma} \\ F_{leg}(\gamma) &= c_{spring}\frac{i\sqrt{j^2 + h^2 - 2jh\cos\gamma}}{j}\left(\frac{(i+h)}{\sqrt{i^2 + h^2 - 2ih\cos\gamma}} - 1\right) \end{aligned} \tag{3.4.1}$$

The error for the parameters $L_0 = 0.16$, $c_{spring} = 4800$ N/m, $\lambda_2 = 0.5$ and $d_{14} = 0.1$ is plotted in Fig. 3.6. The maximal error is $e_{F_{leg}} = \pm 1.0686$ N for $\gamma = 122°$, which corresponds to a relative error of $\pm$ 10.8%. Taking into account that not the entire range of 180° is needed (the leg is never fully compressed), a proper range for the potentiometer can be used. When using a range of 60°, the maximal error is $e_{F_{leg}}$ 0.39 N at $\gamma = 30.7°$, which corresponds to a relative error of $\pm 2.19\%$. For the leg angle η the absolute error remains $e_\eta = \pm 3\%$. As the rotational spring force $F_{spring,rot}$ depends directly on the leg angle, the absolute error for this force is also $e_{F_{spring,rot}} = \pm 3\%$. The damping force depends on $\dot{\eta}$, which needs at least two measurements of η to be evaluated. The worst case for this result is an additive error of $e_\eta = 6\%$. However in steady-state the forces $F_{spring,rot}$ and $F_{damp,rot}$ are negligible for the stance phase (see Fig. 3.7).
At a leg angle at touchdown of $\eta_{td} \approx 60°$ and $\eta_{lo} \approx 120°$ at lift-off, the error of $\pm 3\%$ in the leg angle η corresponds to a mean error of $\pm 1.77\%$ for F_y (sine term) and $\pm 6.48\%$ for F_x (cosine term). The different error for F_x and F_y depends on where $\eta = 0$ is set. The error resulting from the measurement errors of γ and η is of multiplicative form and is about $\pm 14\%$ for F_x and $\pm 3.9\%$ for F_y.
The error for the leg length depends on γ and is $e_L \approx 2\%$.
In the simulation, the system is able to handle errors of $\pm 1\%$ for both the horizontal and vertical acceleration. Especially for the estimation of the horizontal velocity, the estimated error is far beyond the error tolerance of the simulation. Additionaly the error for the horizontal velocity is additive form stride to stride. Therefore the strategy used in simulation will probably not be able to stabilise a similar system in real-world by only using a potentiometer.

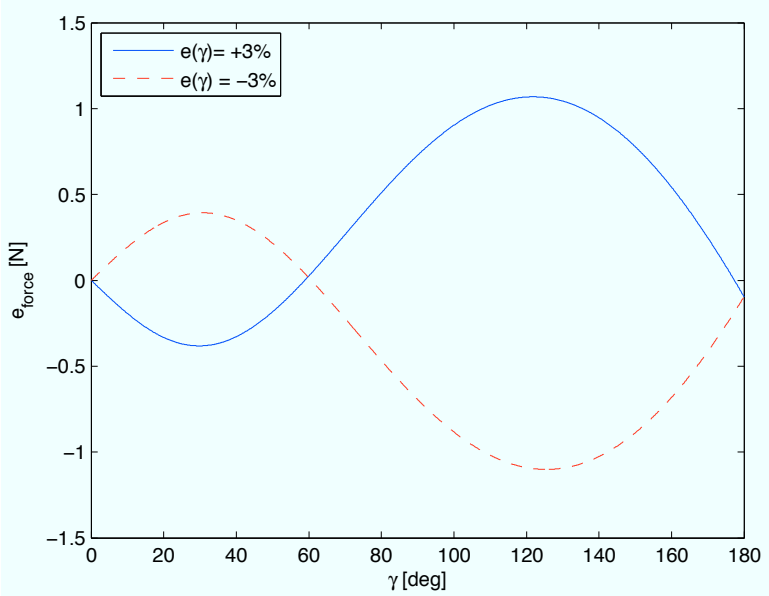

Figure 3.6: The error in the measurement of the leg force F_{leg} depending on the angle γ for the parameters $L_0 = 0.16$, $c_{spring} = 4800$ N/m, $\lambda_2 = 0.5$ and $d_{14} = 0.1$

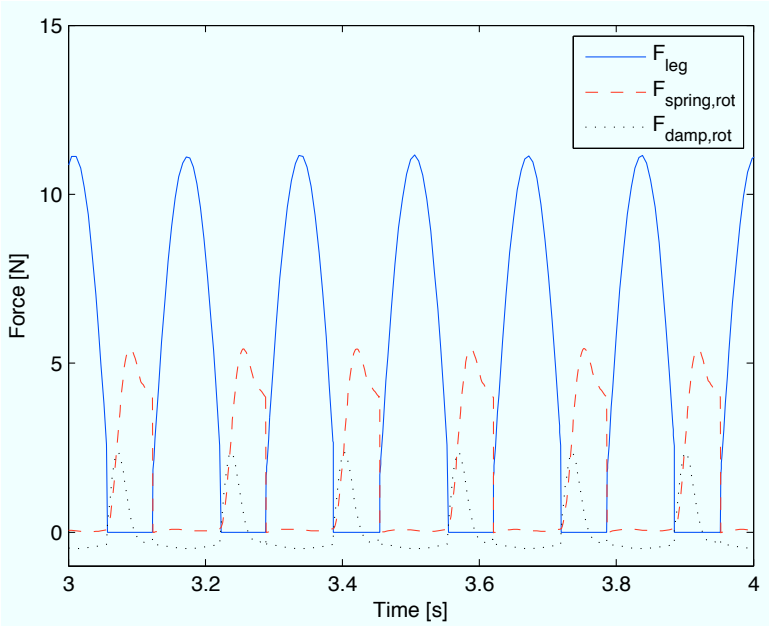

Figure 3.7: Forces acting on the leg in steady-state: blue solid: F_{leg}, red dashed: $F_{spring,rot}$, black dotted: $F_{damp,rot}$. The rotational forces during stance (where $F_{leg} \neq 0$) are small compared to the leg force.

Chapter 4

Discussion

4.1 Energy Conservative System

In chapter 2 the stabilty in running for the pantograph leg is analysed in an energy conservative system. The basic properties of the SLIP model described in [26] can be inherited. The system is able to generate periodic running movements, which are stable for the proper leg parameters and initial conditions. The dependency in the adjustment of angle of attack to leg stiffness for stable running is J-shaped. The pantograph leg does not bring major improvements over the telescopic model. For certain leg geometries (such as $\lambda_2 = 0.5$ and $d_{14} = 0.1$) the regions of stability could be increased and bent such that stable running is possible for a larger band of angles of attack for a given leg stiffness. However the improvement was not as drastic as for example with the two-segmented leg model in [23]. In the latter work it is stated that the degressive effective leg stiffness of the two-segmented leg model causes the improved stabilty. Altough the pantograph leg has (for a proper parameter choice) a degressive leg stiffness, the amounts of leg compression relevant for running are still close to a linear length-force relationship.
An improvement over the spring-mass model brings the preloading of the spring. It allows for stable running at lower speeds and a major band of angles of attack is tolerated for given speeds. The same effect as spring preloading has landing with a precompressed leg ($L_{td} < L_0$). This is useful as L_{td} can easily be adapted online. The preloading might though bring some disadvantages for the real robot which were not investigated due to the simplicity of the physical model. Namely the danger of slipping is increased as the leg force at touchdown is non-zero for a preloaded spring. A major impact at touchdown is further mechanically unfavourable for the joints.

4.2 Controlled System

In chapter 3 the behaviour of the pantograph leg was analysed in a system where the leg angle can be controlled by a motor at the hip. The leg is attached to the motor by a rotational spring. The system was able to achieve stable gaits at low velocities (minimal speed was 0.7 m/s compared to 1.25 m/s for the pantograph leg without preload). The stable running at low speeds is surely supported by the choice of the leg length at touchdown $L_{td} < L_0$, which is equivalent to a preloaded spring. The preloaded pantograph leg in the energy conservative system was though only able to run stable for a minimal speed of $v_{x,0} = 1.1$ m/s for the same amount of preloading. The lower minimal speed might be explained by the influence of the rotational spring on the swing-forward of the leg during flight. The leg has no fixed

angle of attack but swings about the desired value due to the rotational spring. This results in a passive swing-leg retraction similar to [27], which allows for stable running at lower speeds.
The system was stable for a step down of -3 cm, whereas for a step up it managed to overcome 1.5 cm only. The difference might again be due to the swing-leg retraction behaviour. However it might also be because of the choice of the initial conditions or the point where the step was placed, as this was not yet investigated extensively. As stated in section 3.4.2 a potentiometer to measure the leg force for integration might not be sufficient for an accurate speed measurement. An approach that measures the duration of the stance phase or additional sensors (such as a speed sensor) might be necessary.

4.2.1 Outlook

The presented strategy is able to overcome steps and to run stable at low speeds. There might though be a lot of potential for improvement by combining it with strategies such as leg retraction ([27]), leg extension ([8],[9]) or leg stiffening ([11]).

Appendix A

Stability Plots

A.1 Steps-to-Fall Method - Without Preload

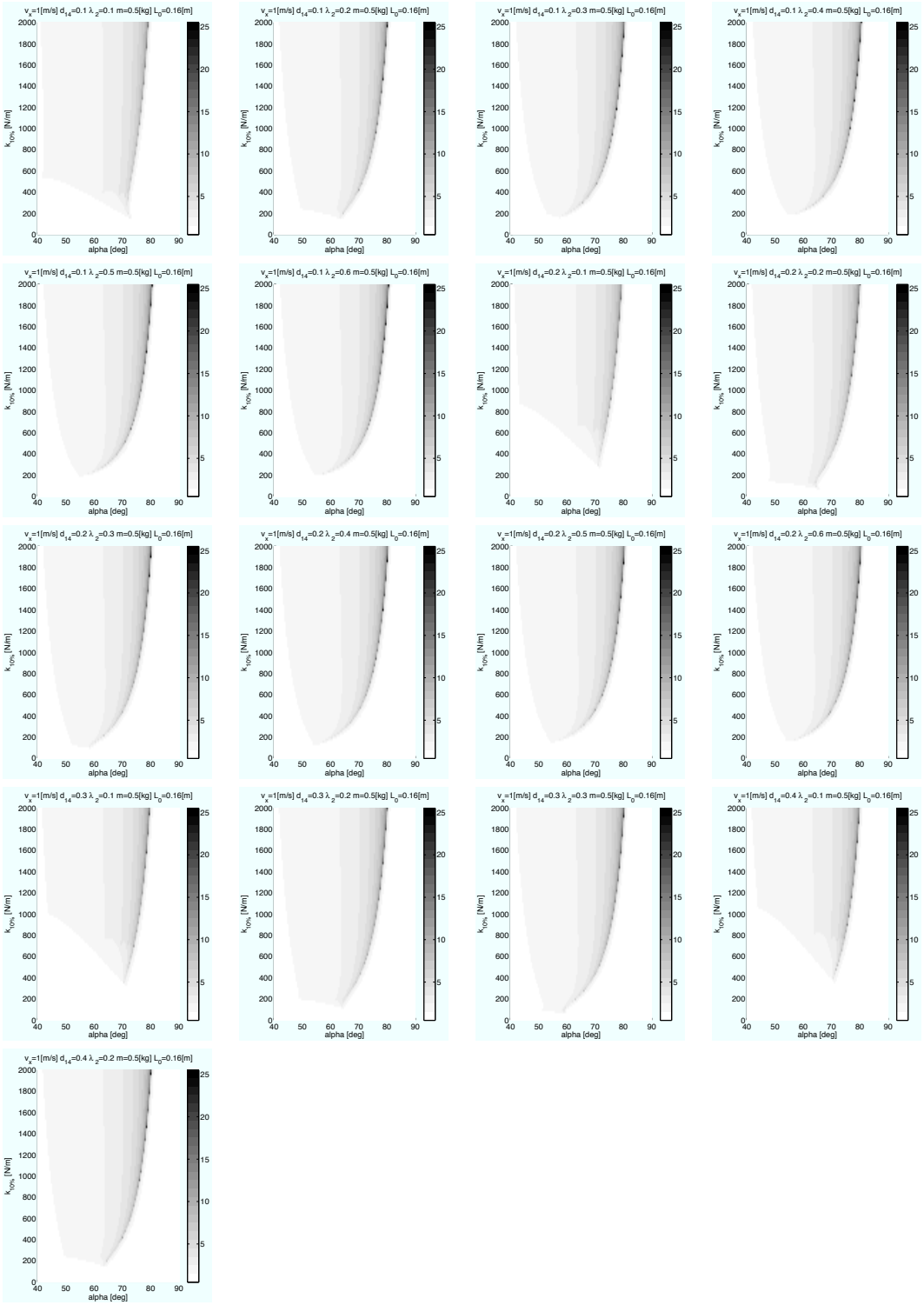

Figure A.1: $v_x = 1.0$ m/s, the stability was tested with the steps-to-fall method

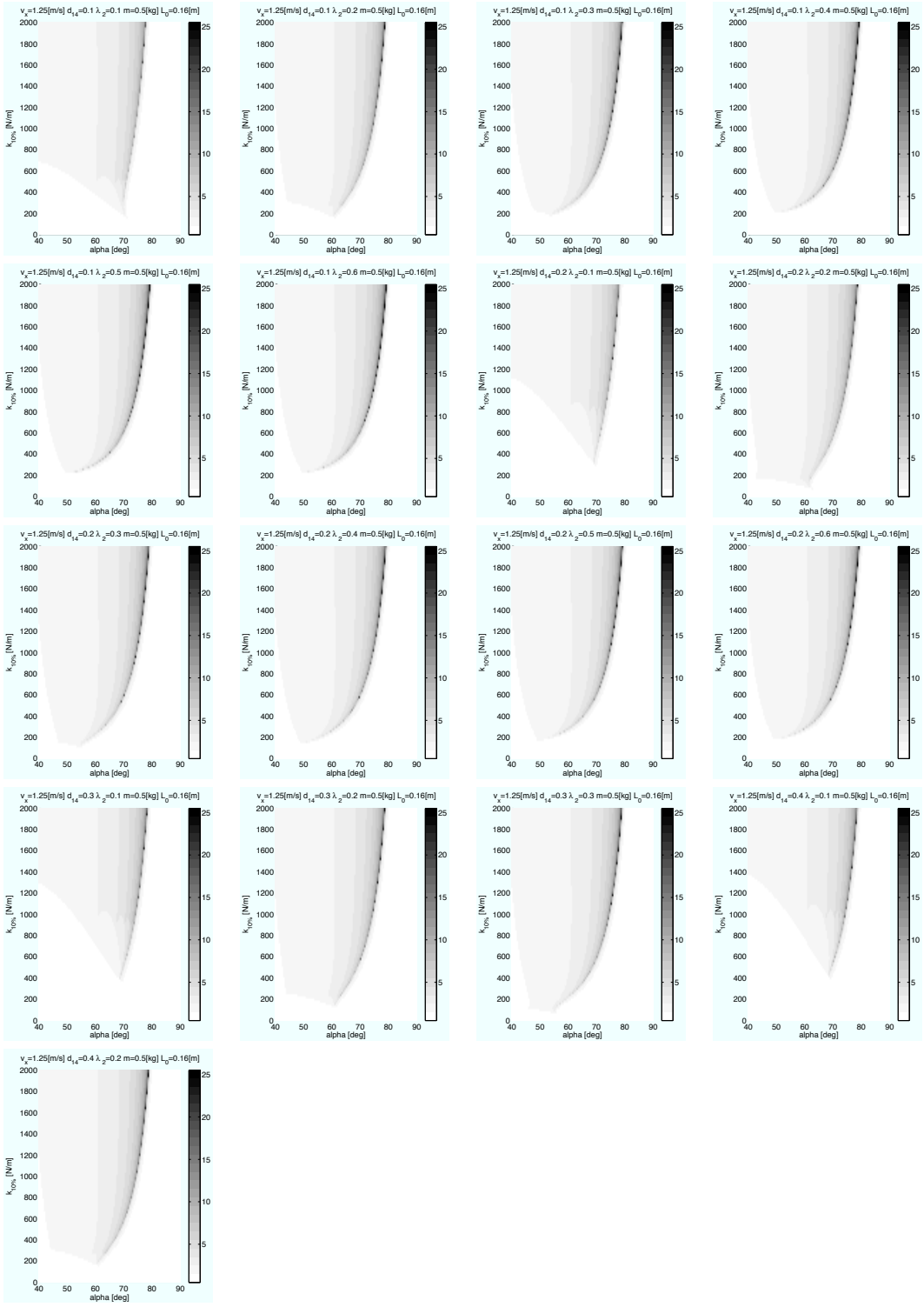

Figure A.2: $v_x = 1.25$ m/s, the stability was tested with the steps-to-fall method

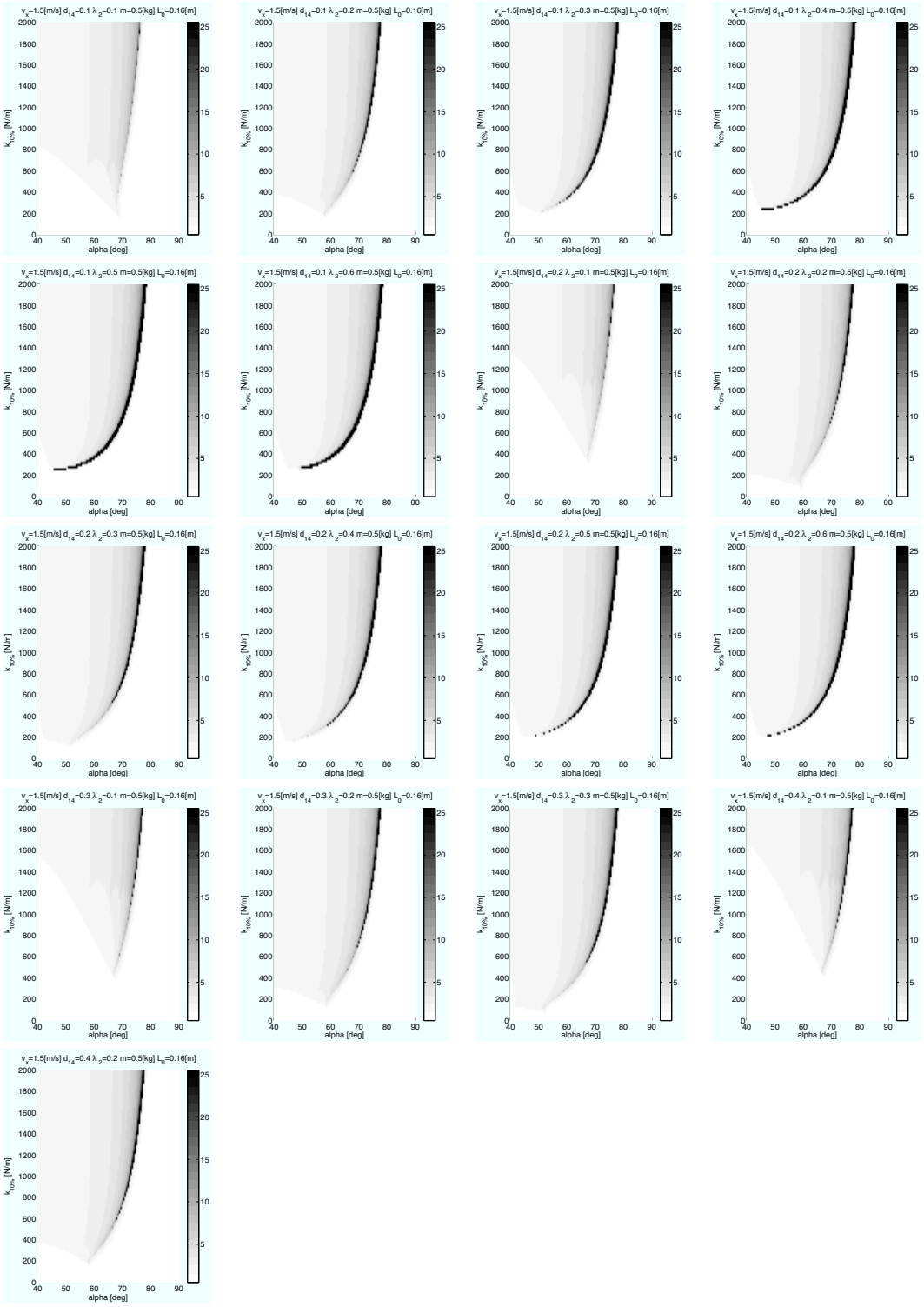

Figure A.3: $v_x = 1.5$ m/s, the stability was tested with the steps-to-fall method

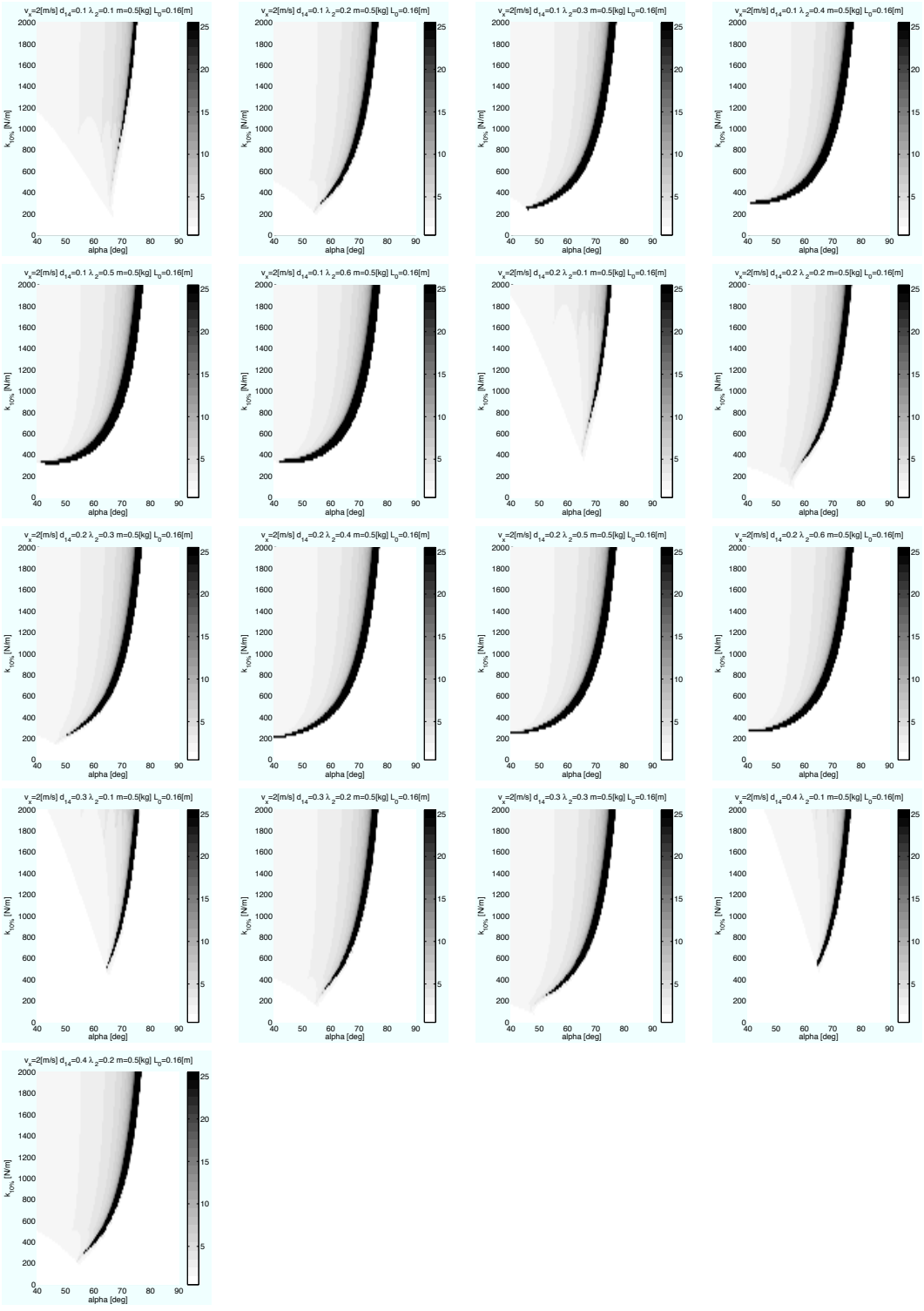

Figure A.4: $v_x = 2.0$ m/s, the stability was tested with the steps-to-fall method

A.2 Apex Return Map - Without Preload

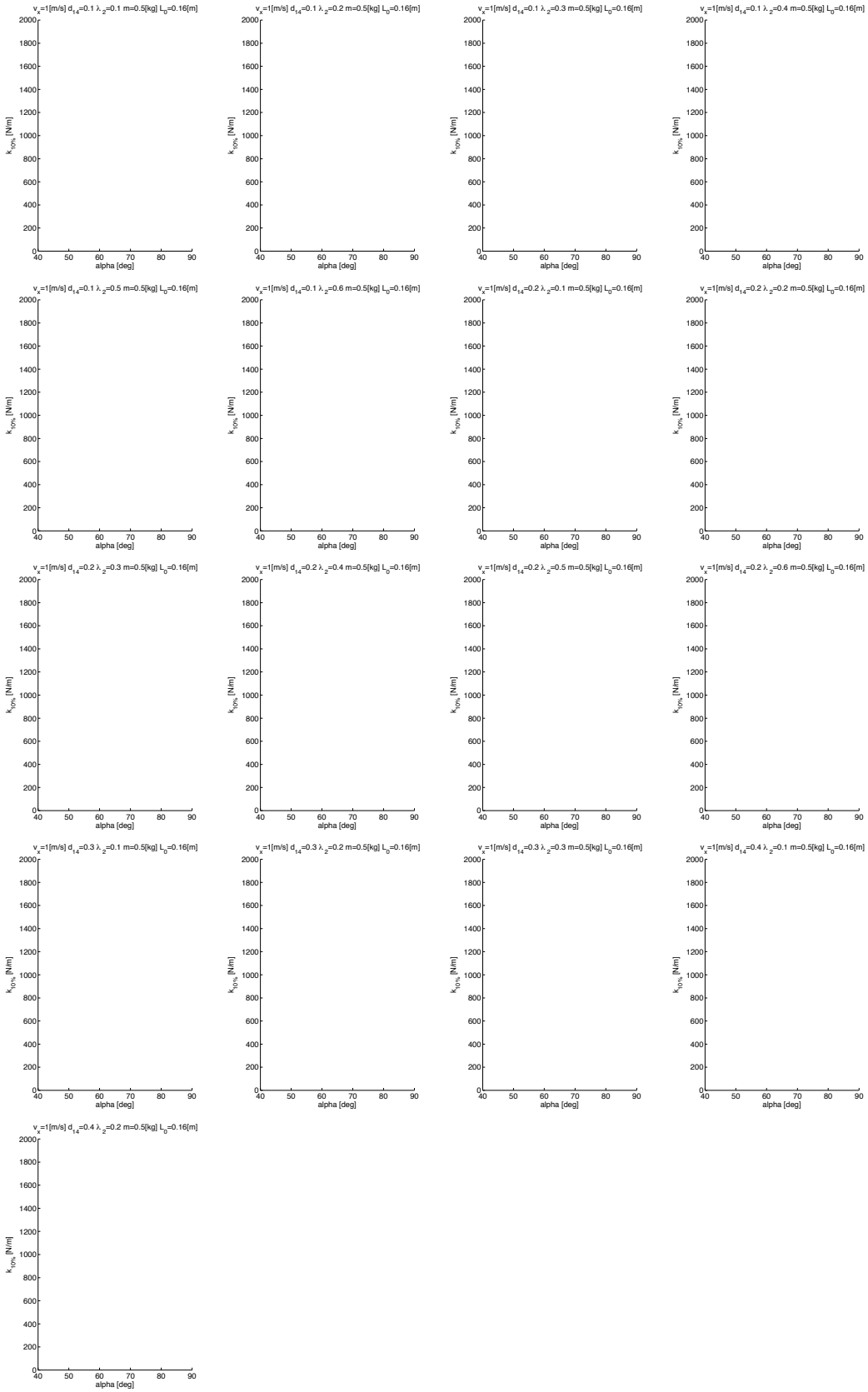

Figure A.5: $v_x = 1.0$m/s, the stability was tested with the apex return map

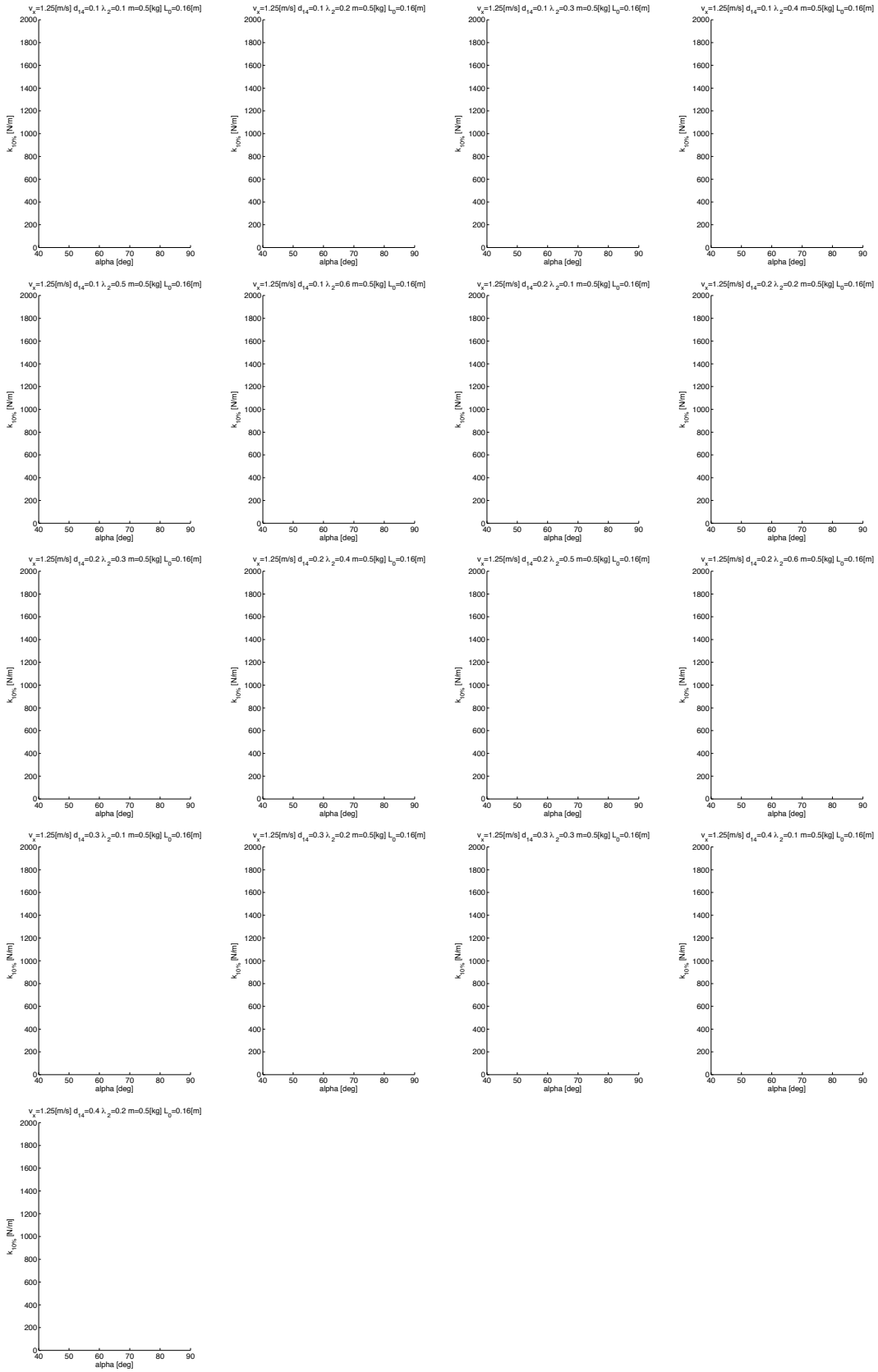

Figure A.6: $v_x = 1.25$m/s, the stability was tested with the apex return map

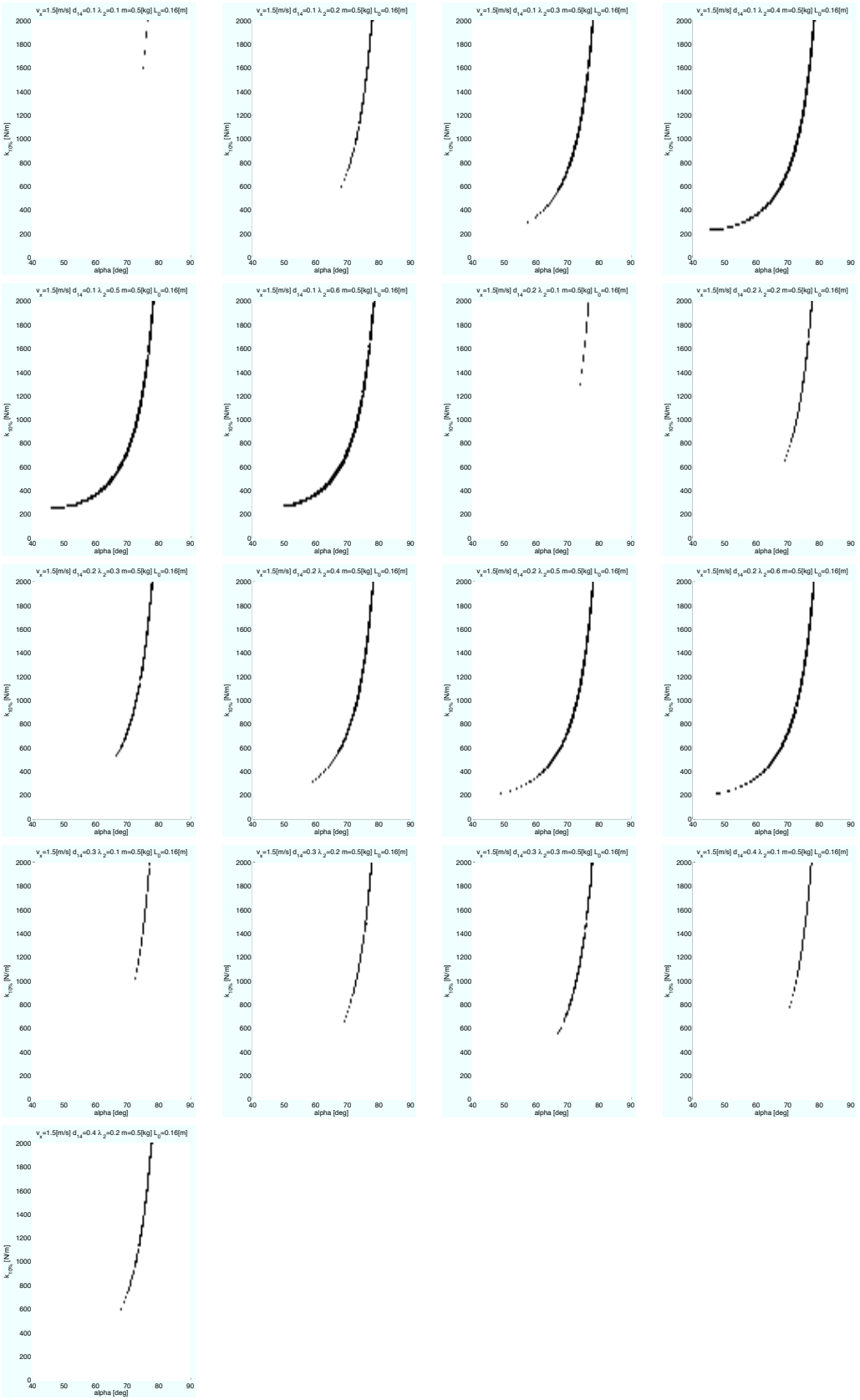

Figure A.7: $v_x = 1.5$m/s, the stability was tested with the apex return map

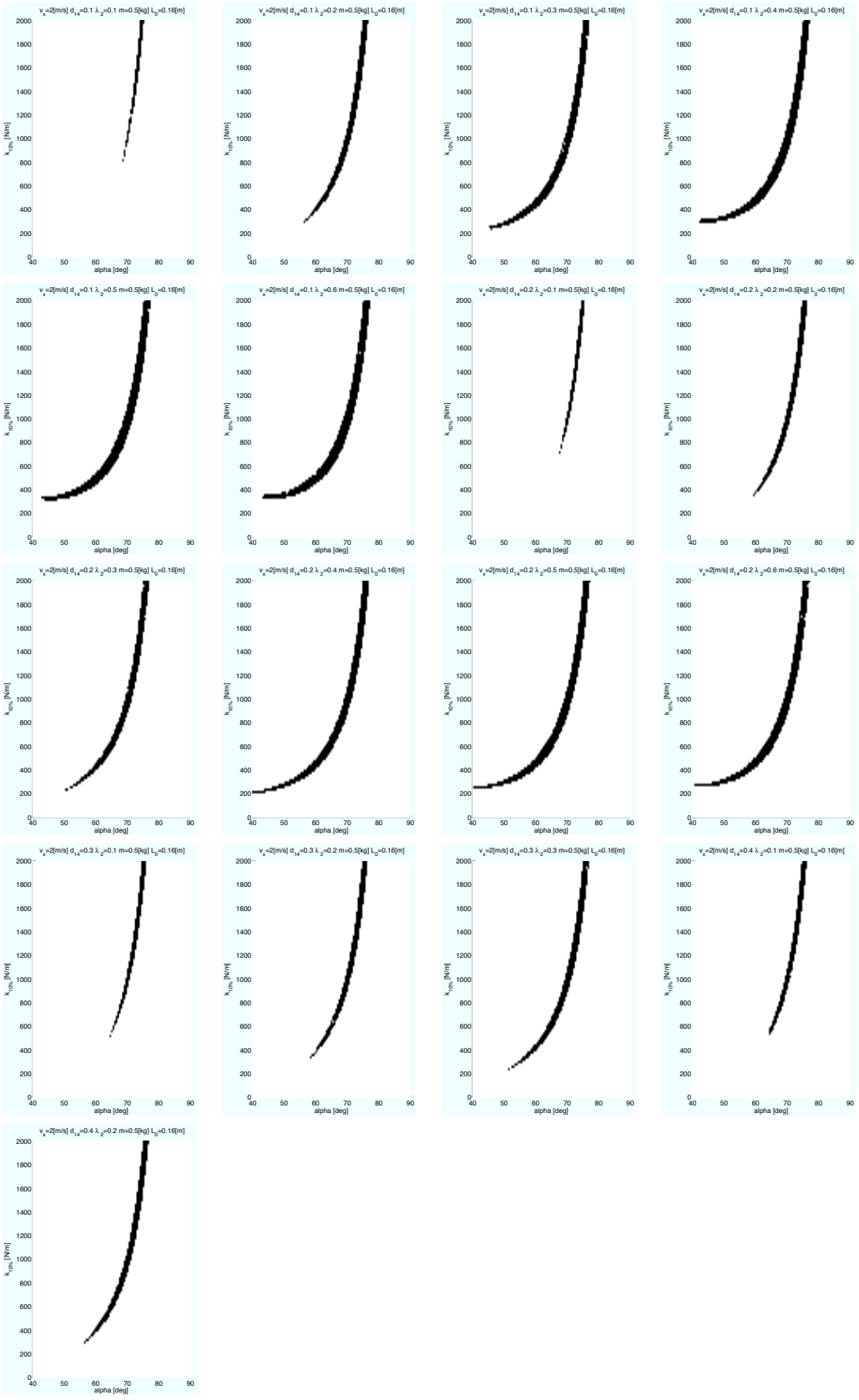

Figure A.8: $v_x = 2.0$ m/s, the stability was tested with the apex return map

A.3 Steps-to-Fall Method - Preloaded

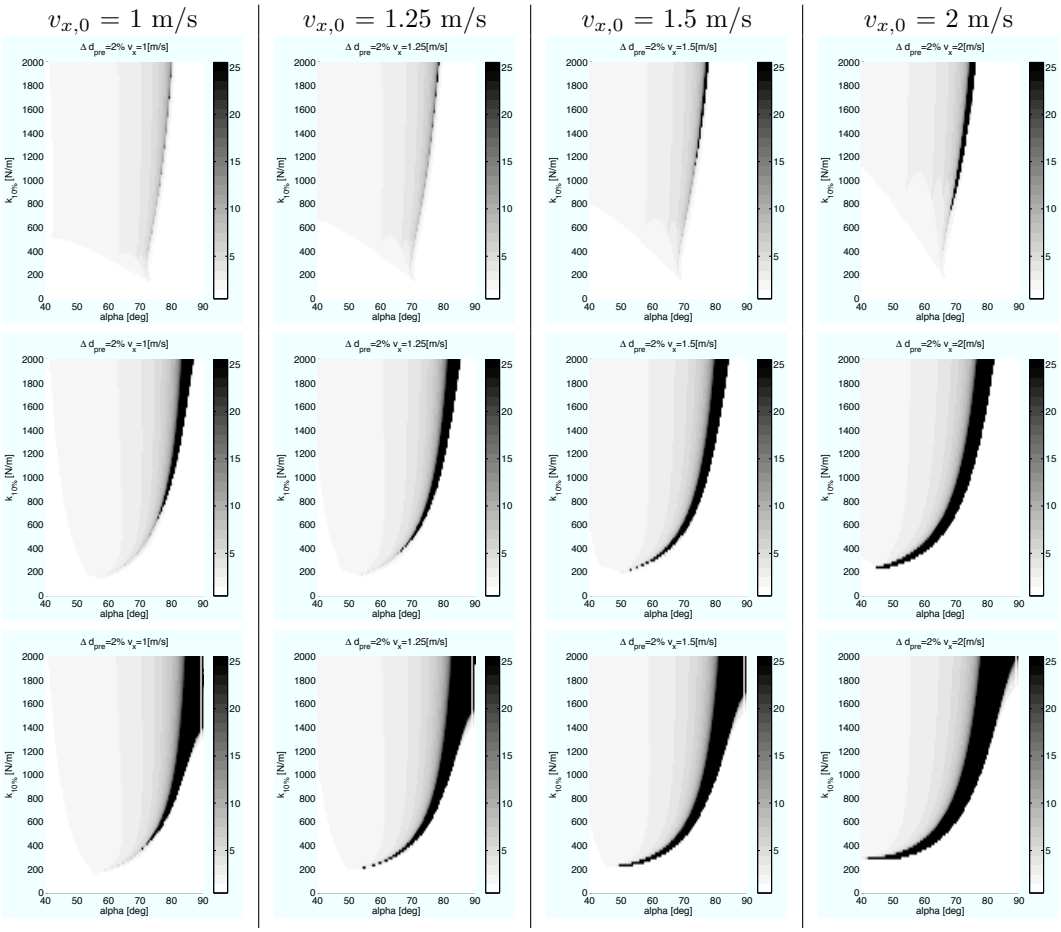

Figure A.9: $\Delta d_{pre} = 2\%$ of the maximal spring length, first row $\lambda_2 = 0.1$, second row $\lambda_2 = 0.3$, third row $\lambda_2 = 0.5$, the stability was tested with the steps-to-fall method

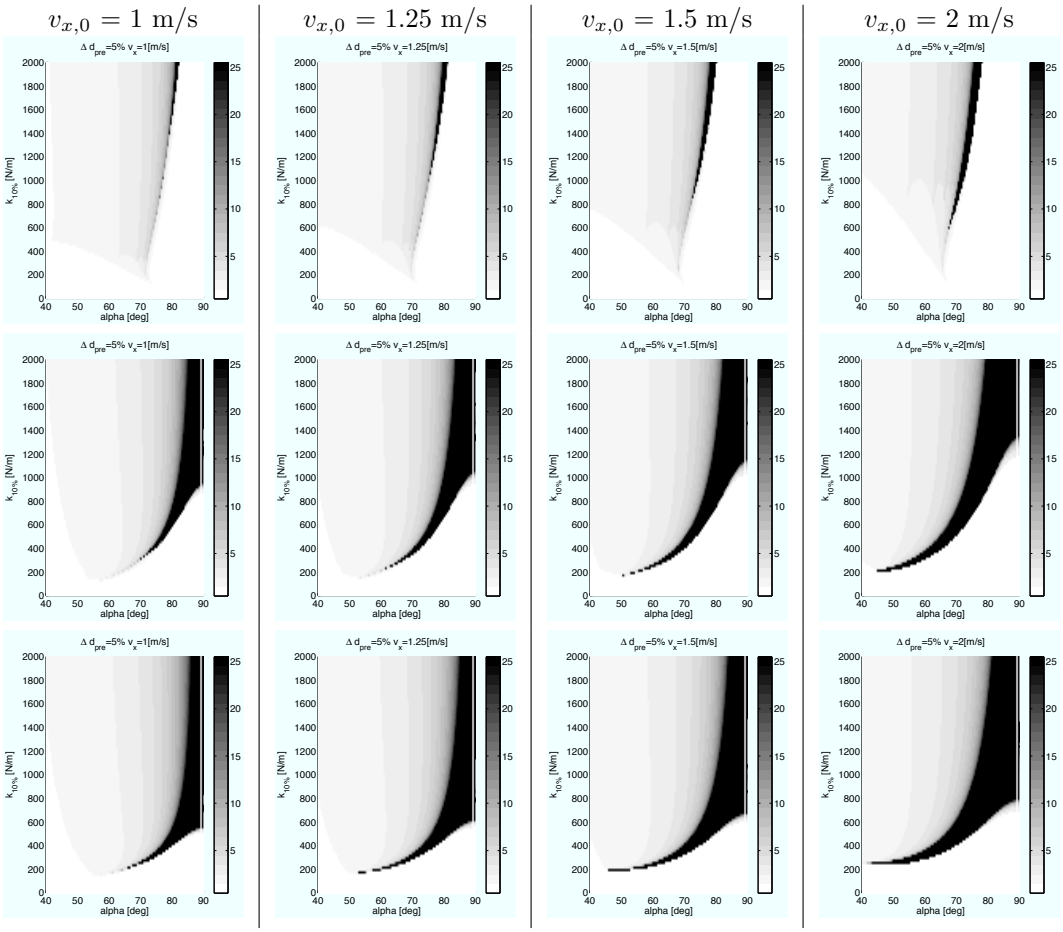

Figure A.10: $\Delta d_{pre} = 5\%$ of the maximal spring length, first row $\lambda_2 = 0.1$, second row $\lambda_2 = 0.3$, third row $\lambda_2 = 0.5$, the stability was tested with the steps-to-fall method

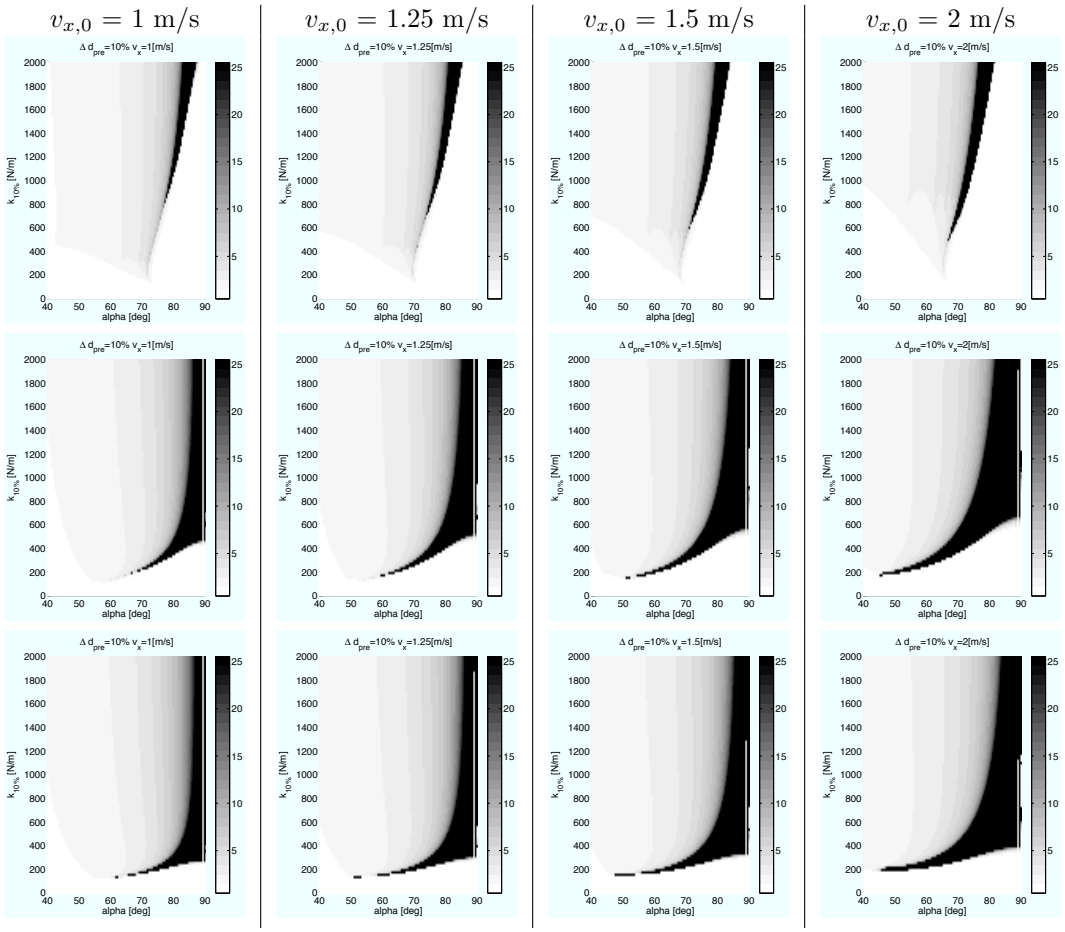

Figure A.11: $\Delta d_{pre} = 10\%$ of the maximal spring length, first row $\lambda_2 = 0.1$, second row $\lambda_2 = 0.3$, third row $\lambda_2 = 0.5$, the stability was tested with the steps-to-fall method

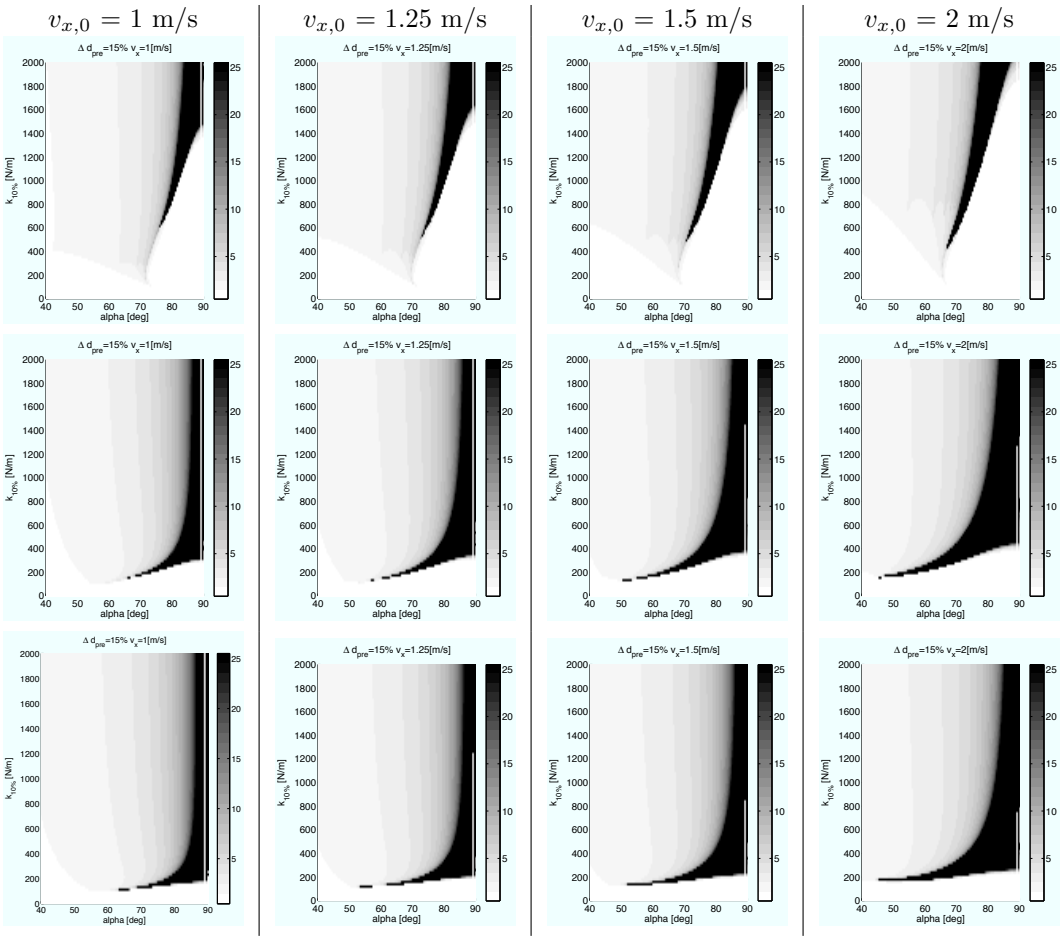

Figure A.12: $\Delta d_{pre} = 15\%$ of the maximal spring length, first row $\lambda_2 = 0.1$, second row $\lambda_2 = 0.3$, third row $\lambda_2 = 0.5$, the stability was tested with the steps-to-fall method

A.4 Apex Return Map - Preloaded

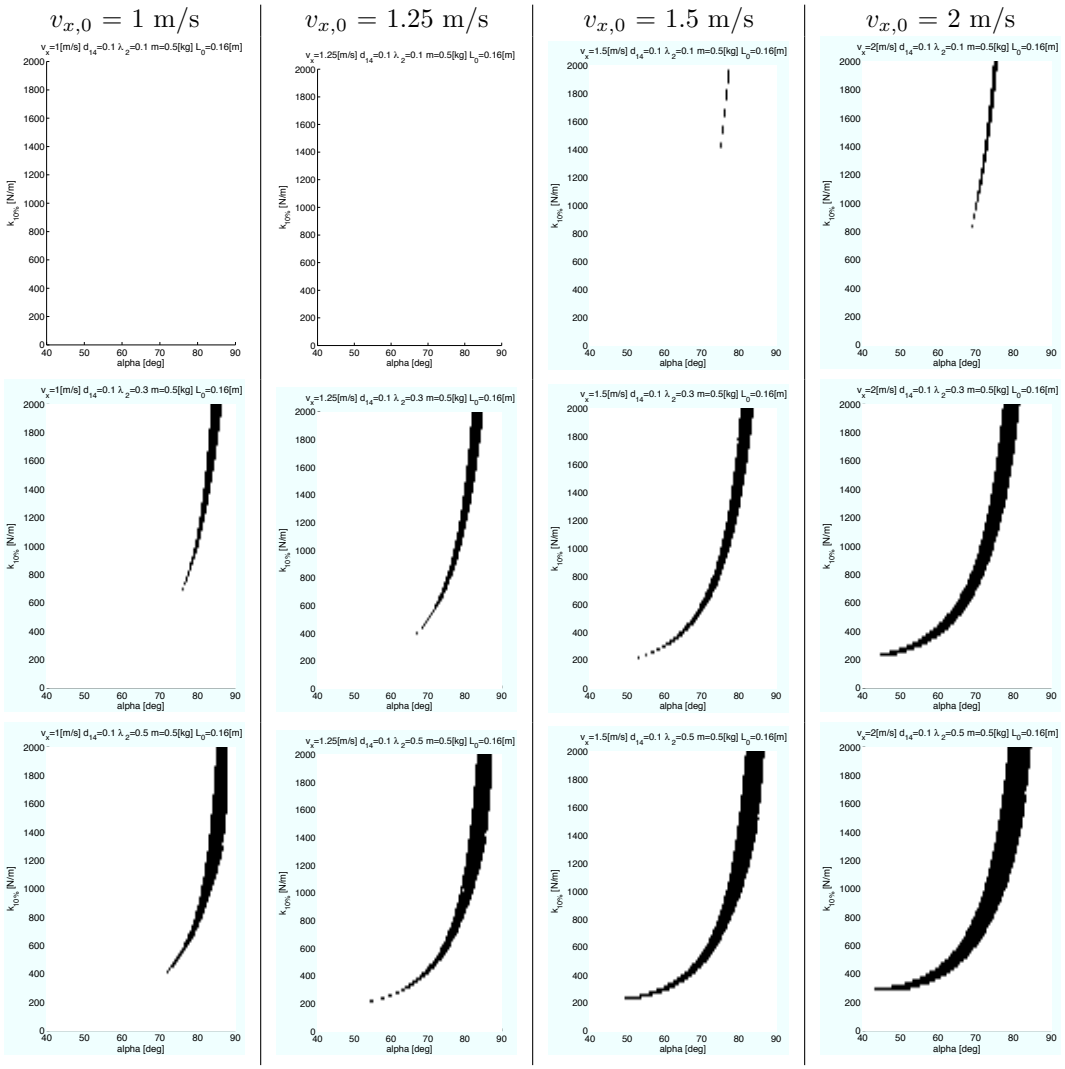

Figure A.13: $\Delta d_{pre} = 2\%$ of the maximal spring length, first row $\lambda_2 = 0.1$, second row $\lambda_2 = 0.3$, third row $\lambda_2 = 0.5$, the stability was tested with the apex return map

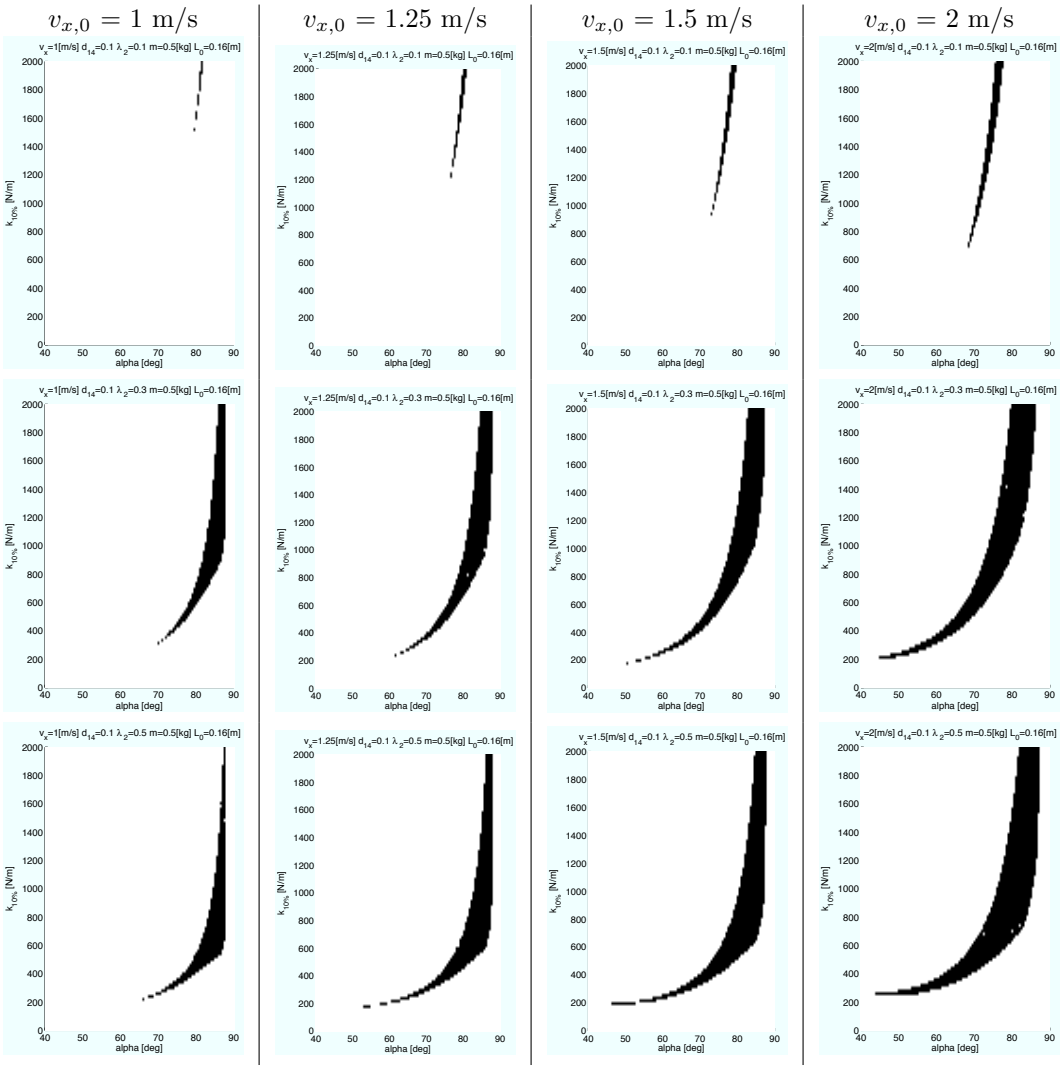

Figure A.14: $\Delta d_{pre} = 5\%$ of the maximal spring length, first row $\lambda_2 = 0.1$, second row $\lambda_2 = 0.3$, third row $\lambda_2 = 0.5$, the stability was tested with the apex return map

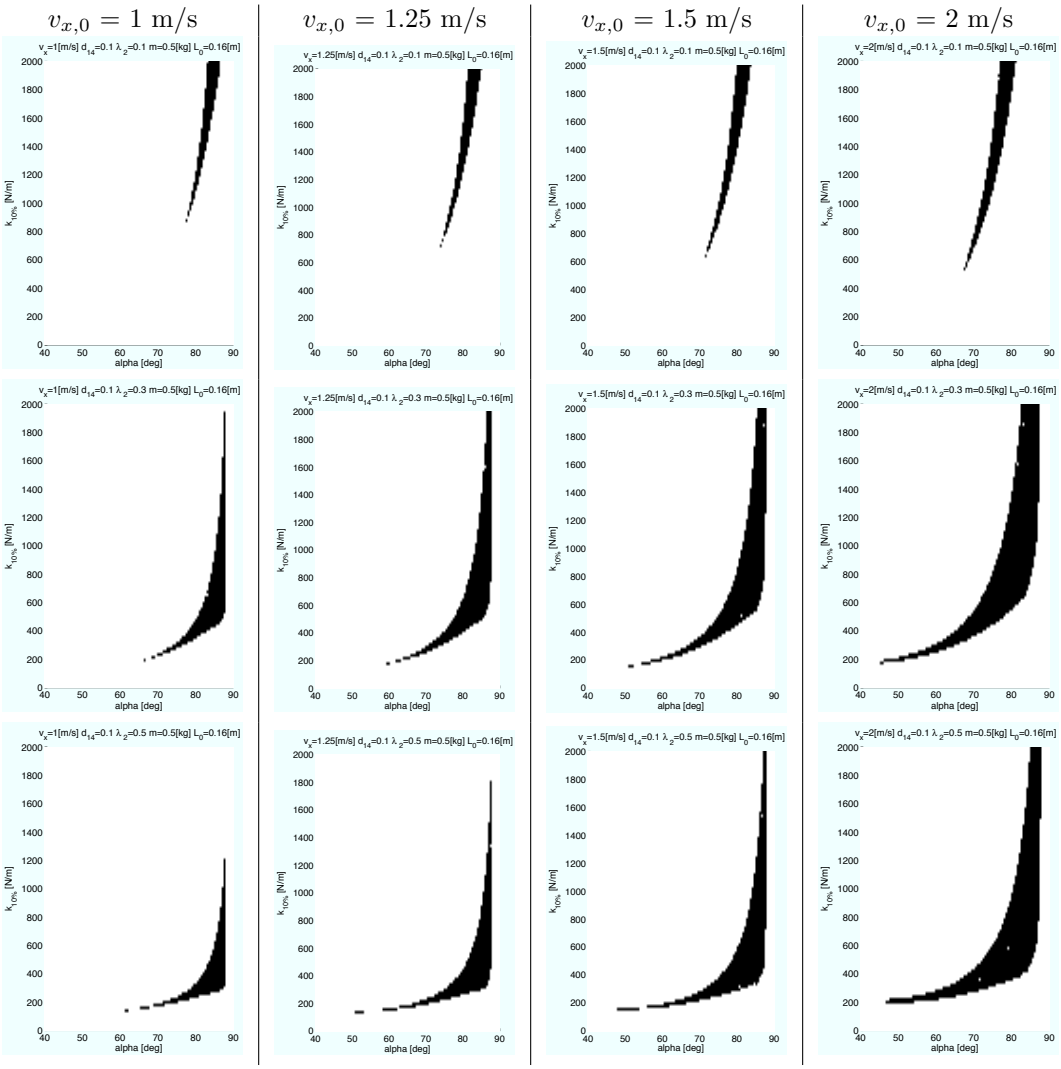

Figure A.15: $\Delta d_{pre} = 10\%$ of the maximal spring length, first row $\lambda_2 = 0.1$, second row $\lambda_2 = 0.3$, third row $\lambda_2 = 0.5$, the stability was tested with the apex return map

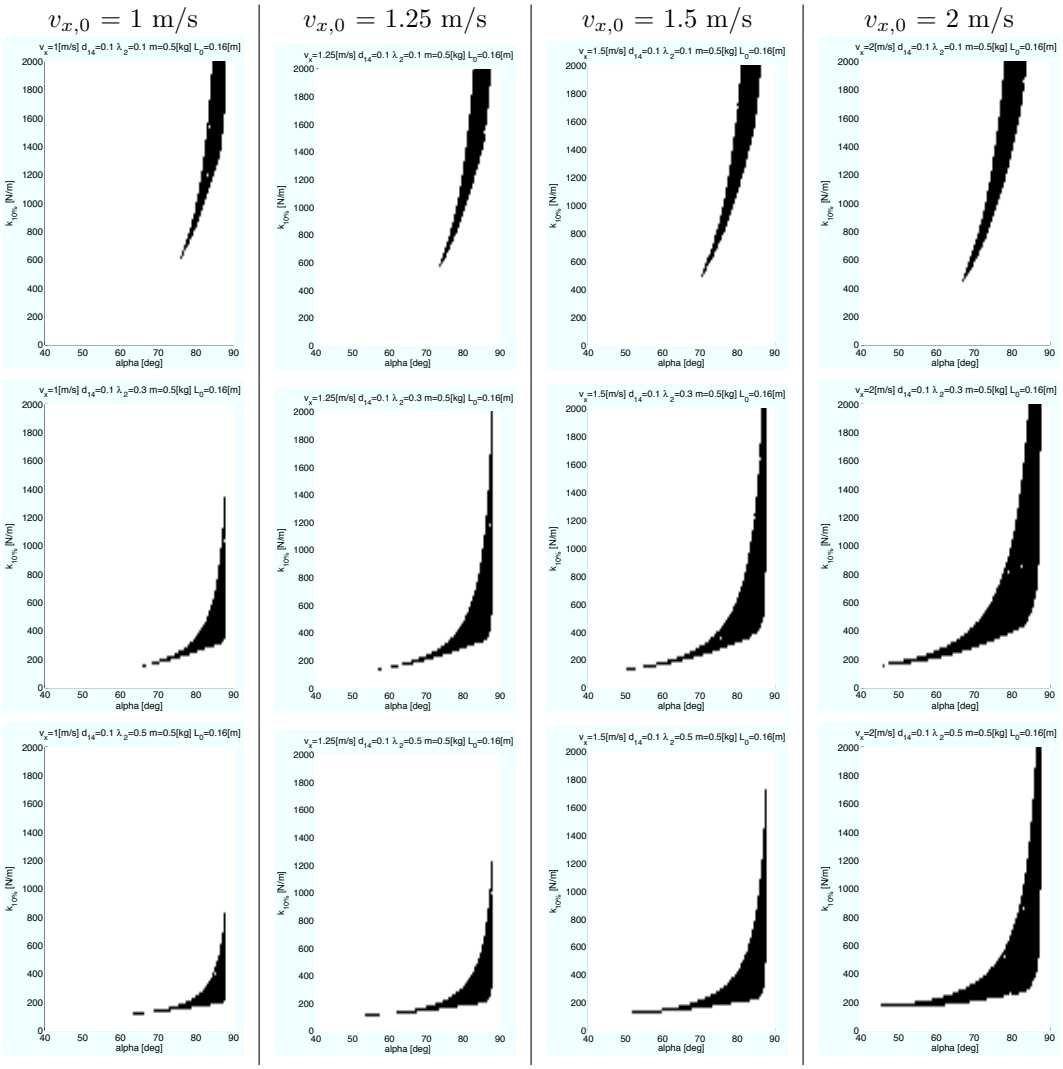

Figure A.16: $\Delta d_{pre} = 15\%$ of the maximal spring length, first row $\lambda_2 = 0.1$, second row $\lambda_2 = 0.3$, third row $\lambda_2 = 0.5$, the stability was tested with the apex return map

Bibliography

[1] http://en.wikipedia.org/wiki/list_of_moments_of_inertia.

[2] http://en.wikipedia.org/wiki/newtons_method.

[3] http://www.piher-nacesa.com/pdf/n15.pdf.

[4] M Ahmadi. Stable control of a simulated one-legged running robot with hip and leg compliance. *IEEE transactions on robotics and automation*, 13(1), 1997.

[5] R. McN. Alexander. The gaits of bipedal and quadrupedal animals. *The International Journal of Robotics Research*, 3(2):49–59, 1984.

[6] Reinhard Blickhan. The spring-mass model for running and hopping. *Journal of Biomechanics*, 22(11-12):1217–1227, 1989.

[7] G A Cavagna. Mechanical work in terrestrial locomotion: two basic mechanisms for minimizing energy expenditure. *American journal of physiology. regulatory, integrative and comparative physiology*, 233(5), 1977.

[8] M A Daley. Running over rough terrain: guinea fowl maintain dynamic stability despite a large unexpected change in substrate height. *The journal of experimental biology*, 209(1), 2006.

[9] Monica A Daley. Biomechanics: running over uneven terrain is a no-brainer. *Curr Biol*, 18(22):R1064–R1066, Nov 2008.

[10] Martin S. Fischer, Nadja Schilling, Manuela Schmidt, Dieter Haarhaus, and Hartmut Witte. Basic limb kinematics of small therian mammals. *Journal of Experimental Biology*, 205(9):1315–1338, 2002.

[11] S Grimmer. Running on uneven ground: leg adjustment to vertical steps and self-stability. *The journal of experimental biology*, 211(18), 2008.

[12] Hobbelen and Wisse. A disturbance rejection measure for limit cycle walkers: The gait sensitivity norm. *IEEE Transactions on Robotics*, 2007.

[13] Y Hurmuzlu. On the measurement of dynamic stability of human locomotion. *Journal of biomechanical engineering*, 116(1), 1994.

[14] A.P. Marsh J.A. Norris and K.P. Granata. Positive feedback in powered-exoskeletons: improved metabolic efficiency at the cost of reduced stability? *Proceedings of the ASME international design engineering technical conferences*, 2007.

[15] Karssen and Wisse. Non-linear leg spring increases the disturbance rejection during running. *Dynamic Walking*, 2009.

[16] Ivan Kviatkevitch. Locomotion exploiting body dynamics on the cheetah robot. Technical report, Biologically Inspired Robotic Group, 2009.

[17] T. McGeer. Passive bipedal running. *Proceedings of the Royal Society of London. Series B, Biological Sciences*, 240(1297):107–134, 1990.

[18] T. McGeer. Passive dynamic walking. *International Journal of Robotics Research*, 9(2):62–82, Apr 1990.

[19] T. McGeer. Passive walking with knees. In *Robotics and Automation, 1990. Proceedings., 1990 IEEE International Conference on*, pages 1640–1645 vol.3, May 1990.

[20] T A McMahon and G.C Cheng. The mechanics of running: How does stiffness couple with speed? *Journal of Biomechanics*, 23(SUPPL. 1):65–78, 1990.

[21] M H Raibert. *Legged robots that balance*. 1986.

[22] M. Riess. Development and test of a model for the cheetah robot. Technical report, Biologically Inspired Robotic Group, 2008.

[23] Juergen Rummel and Andre Seyfarth. Stable running with segmented legs. *The International Journal of Robotics Research*, 27(8):919–934, August 2008.

[24] S. Rutishauser. Cheetah: compliant quadruped robot. Technical report, Biologically Inspired Robotic Group, 2008.

[25] Simon Rutishauser, Alexander Sproewitz, Ludovic Righetti, and Auke Jan Ijspeert. Passive compliant quadruped robot using central pattern generators for locomotion control. In *2008 IEEE International Conference on Biomedical Robotics and Biomechatronics*, 2008.

[26] A Seyfarth. A movement criterion for running. *Journal of Biomechanics*, 35(5), 2002.

[27] A Seyfarth. Swing-leg retraction: a simple control model for stable running. *The journal of experimental biology*, 206(15), 2003.

[28] Alexander Spröwitz, Simon Rutishauser, and Auke Jan Ijspeert. Compliant quadruped robot cheetah passive and active leg mechanics. Biologically Inspired Robotics Group, EPFL, Switzerland, 2009.

[29] H Witte, R Hackert, W Ilg, J Biltzinger, N Schilling, F Biedermann, M Jergas, H Preuschoft, and M S Fischer. Quadrupedal mammals as paragons for walking machines. In *International Symposium on Adaptive Motion in Animals and Machines (AMAM)*, 2000.